View metadata, citation and similar papers at core.ac.uk
brought to you by CORE
provided by DSpace@MIT

INTERNATIONAL JOURNAL FOR NUMERICAL METHODS IN ENGINEERING
Int. J. Numer. Meth. Engng 0000; **00**:1–29
Published online in Wiley InterScience (www.interscience.wiley.com). DOI: 10.1002/nme

A finite-element implementation of the nonlocal granular rheology

David L. Henann[1*] and Ken Kamrin[2]

[1]*School of Engineering, Brown University*
[2]*Department of Mechanical Engineering, MIT*

SUMMARY

Inhomogeneous flows involving dense particulate media display clear size effects, in which the particle length scale has an important effect on flow fields. Hence, nonlocal constitutive relations must be used in order to predict these flows. Recently, a class of nonlocal fluidity models have been developed for emulsions and subsequently adapted to granular materials. These models have successfully provided a quantitative description of experimental flows in many different flow configurations. In this work, we present a finite-element-based numerical approach for solving the nonlocal constitutive equations for granular materials, which involve an additional, non-standard nodal degree-of-freedom – the granular fluidity, which is a scalar state parameter describing the susceptibility of a granular element to flow. Our implementation is applied to three canonical inhomogeneous flow configurations: (i) linear shear with gravity, (ii) annular shear flow without gravity, and (iii) annular shear flow with gravity. We verify our implementation, demonstrate convergence, and show that our results are mesh-independent. Copyright © 0000 John Wiley & Sons, Ltd.

Received . . .

KEY WORDS: Granular materials; Nonlocal rheology; Finite-element method

1. INTRODUCTION

Dense, amorphous, particulate media – such as concentrated emulsions, foams, suspensions, and granular materials – appear frequently in engineering applications as well as in everyday life. When subjected to homogeneous simple shear, these materials display a complex, non-linear mechanical response. First, a distinct yield condition is observed, and hence, there are a set of stress states for which only elastic deformation occurs. Beyond the yield point, rate-dependent, or viscoplastic, flow occurs. Constitutive equations – such as the Herschel-Bulkley model for emulsions or dense suspensions or the inertial rheology for granular materials [1, 2, 3, 4] – have been successful at describing this homogeneous response. However, for inhomogeneous flows, this approach breaks down. The stress at a point is no longer given through local constitutive equations involving strain, strain rate, or locally-evolved state variables. As a consequence, flows involving these materials display finite-size effects, in which the ratio of the characteristic size of the flow configuration to the particle size has an important impact on the observed flow fields [1, 5, 6, 7]. This is evidence that the aforementioned size-independent constitutive relations are insufficient for describing inhomogeneous flows, and developing nonlocal, continuum-level constitutive equations has posed a substantial challenge in engineering and condensed matter physics.

At a microscopic level, the origin of the size-dependence observed during flow is the cooperativity of the building-block particles – droplets in emulsions, bubbles in foams, or grains in granular media. In essence, a plastic rearrangement of a cluster of particles at one spatial position is not

*Correspondence to: 182 Hope St., Box D, Providence, RI 02906, USA. E-mail: david_henann@brown.edu

Copyright © 0000 John Wiley & Sons, Ltd.

only driven by the stress felt by that cluster but is also affected by rearrangements of neighboring particles clusters. Hence, incorporating this notion of cooperativity is a crucial aspect of developing predictive continuum equations. Recently, a nonlocal continuum model for dense particulate flows was developed by Bocquet and coworkers [8, 6, 9, 10] – called the kinetic elastoplastic (KEP) model – that accounts for cooperative effects. Their approach begins with a model for the microscopic dynamics of particle clusters – an approach similar to soft glassy rheology (SGR) [11] – which accounts for local elastic loading and plastic rearrangements as well as the nonlocal redistribution of stress due to local plastic events. The microscopic dynamics are then coarse-grained to the macroscale, resulting in a set of continuum-level constitutive equations. Importantly, their approach identifies a scalar order parameter – the fluidity – which represents the rate of plastic rearrangements, and the continuum-level constitutive equations involve gradients of this order parameter. The inclusion of fluidity gradients in the constitutive equations renders them scale-dependent, and these equations were shown to quantitatively account for the size-effects seen in flows of dense emulsions through microchannels [6, 10] as well as annular shear flow of foams [12].

The microscopic picture in granular materials is analogous, albeit modified for the effect of pressure arising due to the frictional contacts between hard (stiff) grains, and our previous work has adapted the nonlocal fluidity concept from pressure-insensitive materials to pressure-sensitive granular media [13, 14, 15], which we highlight here. The approach begins with a description of flow in steady, homogeneous simple shearing – the local inertial rheology [2, 3, 4]. Consider a dry granular system made up of hard, quasi-monodisperse, spherical grains with mean grain diameter d and grain material density ρ_{s}. The local rheology then relates the shear stress, $\bar{\tau}$, and the pressure, $\bar{p}$, to the shear plastic strain rate $\dot{\gamma}^{\mathrm{p}}$ (defined in general later in Eqs. (11) and (19), respectively). Basic dimensional analysis applied to this case leads to two dimensionless groups: the inertial number, $I = \dot{\gamma}^{\mathrm{p}}\sqrt{d^2\rho_{\mathrm{s}}/\bar{p}}$, and the stress ratio, $\mu = \bar{\tau}/\bar{p}$, which are then related through a one-to-one functional dependence. The simplest form of this functional relation, which is consistent with data [2], is a linear Bingham-like form, $\mu_{\mathrm{loc}}(I) = \mu_{\mathrm{s}} + bI$, where μ_{s} is a dimensionless, static yield value, and b is a dimensionless material parameter of order one that describes the granular material's rate dependence beyond yield. This local relation may be inverted to give a local constitutive equation for the shear plastic strain rate

$$\dot{\gamma}^{\mathrm{p}}_{\mathrm{loc}}(\bar{p},\mu) = \begin{cases} \sqrt{\bar{p}/\rho_{\mathrm{s}}d^2}\,(\mu-\mu_{\mathrm{s}})/b & \text{if } \mu > \mu_{\mathrm{s}}, \\ 0 & \text{if } \mu \leq \mu_{\mathrm{s}}. \end{cases} \tag{1}$$

Then, the model introduces a scalar order parameter characterizing the flow, called the granular fluidity, g – a field variable which relates the stress quantity that drives flow, μ, to the consequent shear plastic strain rate, i.e.,

$$\dot{\gamma}^{\mathrm{p}} = g\mu. \tag{2}$$

The local rheology (1) may be used to define a local functional form for the fluidity, $g_{\mathrm{loc}}(\bar{p},\mu) = \dot{\gamma}^{\mathrm{p}}_{\mathrm{loc}}(\bar{p},\mu)/\mu$. Finally, following Bocquet [9], to account from the observed deviation from a local description (1), the nonlocal granular fluidity model utilizes the following differential constitutive relation which involves gradients in the granular fluidity:

$$\nabla^2 g = \frac{1}{\xi^2}(g - g_{\mathrm{loc}}), \tag{3}$$

where $\xi(\mu)$ is the stress-dependent cooperativity length and $\nabla^2(\cdot)$ represents the Laplacian operator. For homogeneous flow, the relation (3) reduces to the local description $g = g_{\mathrm{loc}}$, but in the presence of gradients, the Laplacian term accounts for nonlocal effects and allows for a quantitative prediction of experimental granular flows [14]. The same model has also been successfully applied to the phenomenology of secondary rheology in granular flows [16]. We note that our nonlocal approach is related to, but distinct from, both explicit [17, 18, 19, 20] and implicit [21, 22] strain gradient plasticity in that gradients in our model are taken over a scalar state parameter rather than a history variable, such as the plastic strain or strain-like variable. Our nonlocal model is also distinct from Cousserat, or micropolar, approaches [23, 24, 25] in that rotational degrees of freedom are not

Copyright © 0000 John Wiley & Sons, Ltd.
Prepared using nmeauth.cls

DOI: 10.1002/nme

utilized. Finally, the model is fully continuum, in contrast to hybrid discrete element/continuum methods [26].

Nonlocal fluidity models have now enjoyed broad success in modeling an array of phenomenologies in several dense particulate systems. However, the mathematical system of equations is non-standard, and solving these equations in arbitrary flow configurations presents a new challenge. The purpose of this paper is to report on our finite-element-based approach to solving boundary-value problems with the nonlocal granular rheology, which we have utilized in our past work [14, 16], and show that our approach is robust. Several specific questions that arise in formulating a finite-element implementation are

- What fields will be interpolated and used to define nodal degrees of freedom?
- What level of continuity is required for the interpolation?
- How will new, non-standard residuals be defined?
- How will the constitutive model be integrated in time and algorithmically consistent tangents be derived?

We will focus on our numerical procedures for pressure-dependent granular materials, since that has been the subject of our previous work. However, the nonlocal fluidity model for pressure-insensitive materials is a simpler case, and appropriate numerical procedures may be straightforwardly deduced from the reported approach. Further, a goal of this paper is to enable a broad community of researchers working on granular flow to utilize our model. To this end, the reported numerical procedures are implemented in Abaqus/Standard [27] using user-element (UEL) subroutines, and the Abaqus UEL subroutines and input files used in this work may be found online as supporting information.

The paper is organized as follows. In Section 2, we recap the nonlocal granular fluidity model in its full three-dimensional, finite-deformation, elasto-plastic form. Then, in Section 3, we detail our finite-element formulation. The finite-element procedures require two additional ingredients: a time-integration procedure and algorithmically-consistent tangents, which are derived in Sections 4 and 5, respectively. Finally, in Section 6, we apply the numerical simulation capability to three canonical granular flow problems: (i) linear shear flow with gravity, (ii) annular shear flow without gravity, and (iii) annular shear flow with gravity. Through these solutions, we verify the implementation and demonstrate convergence and mesh-independence.

2. SUMMARY OF THE MODEL

We begin by summarizing the nonlocal granular rheology for steady, dense granular flow. The theory is three-dimensional, accounts for finite-deformations, and allows for both reversible elastic deformation and nonlocal plastic flow. For a detailed, thermodynamically-consistent derivation based on the principle of virtual power, see our previous work [15].

Kinematics: Consider a body B in a fixed reference configuration and denote arbitrary material points in B by $\mathbf{X}$. The referential body B then undergoes a motion $\mathbf{x} = \boldsymbol{\chi}(\mathbf{X}, t)$ to the deformed body $\mathcal{B}_t$. The theory involves the following kinematical fields:† $\mathbf{F} = \nabla\boldsymbol{\chi}$, $J = \det\mathbf{F} > 0$ deformation gradient; $\mathbf{F} = \mathbf{F}^{\mathrm{e}}\mathbf{F}^{\mathrm{p}}$, multiplicative elastic-plastic decomposition of $\mathbf{F}$ [29, 30]; $\mathbf{F}^{\mathrm{p}}$, $J^{\mathrm{p}} = \det\mathbf{F}^{\mathrm{p}} > 0$, plastic distortion; and $\mathbf{F}^{\mathrm{e}}$, $J^{\mathrm{e}} = \det\mathbf{F}^{\mathrm{e}} > 0$, elastic distortion. The right polar decomposition of $\mathbf{F}^{\mathrm{e}}$ is

$$\mathbf{F}^{\mathrm{e}} = \mathbf{R}^{\mathrm{e}}\mathbf{U}^{\mathrm{e}}, \tag{4}$$

†Our notational conventions follow those of Gurtin [28]. The symbols ∇ (or equivalently $\partial(\cdot)/\partial\mathbf{X}$) and Div denote the gradient and divergence with respect to the material point $\mathbf{X}$ in the reference configuration; grad (or $\partial(\cdot)/\partial\mathbf{x}$) and div denote these operators with respect to the point $\mathbf{x} = \boldsymbol{\chi}(\mathbf{X}, t)$ in the deformed configuration. A superposed dot denotes the material time-derivative. Throughout, we write sym $\mathbf{A}$, skw $\mathbf{A}$, and $\mathbf{A}_0$ for the symmetric, skew, and deviatoric parts of a tensor $\mathbf{A}$, respectively. Also, the inner product of tensors $\mathbf{A}$ and $\mathbf{B}$ is denoted by $\mathbf{A} : \mathbf{B}$, and the magnitude of $\mathbf{A}$ by $|\mathbf{A}| = \sqrt{\mathbf{A} : \mathbf{A}}$.

Copyright © 0000 John Wiley & Sons, Ltd.

Prepared using nmeauth.cls
DOI: 10.1002/nme

where $\mathbf{R}^{\mathrm{e}}$ is a proper rotation tensor and $\mathbf{U}^{\mathrm{e}}$ is the symmetric, positive-definite right stretch tensor.

In our previous work [15], we made the assumption of small elastic strains in the development of our theory – a reasonable approximation that led to considerable simplification – and left the details of the elastic response unspecified. Implementing the model in a large-deformation framework requires us to make concrete choices regarding the elastic response. Most notably, we must adopt a large-deformation elastic strain measure – which was inconsequential in a small-deformation framework. To this end, we utilize the Hencky (logarithmic) elastic strain measure:

$$\mathbf{E}^{\mathrm{e}} = \ln \mathbf{U}^{\mathrm{e}}. \tag{5}$$

This choice is motivated by the time-integration procedure that we develop in Section 4, which is based upon the exponential map and hence works particularly well when the logarithmic elastic strain is employed. We emphasize that in the steady-flow setting for which the model is intended, this choice does not affect the predictivity of the model. That is to say, we would obtain the same steady flow predictions using the Green strain, Almansi strain, etc.

We next define the velocity and spatial velocity gradient by $\mathbf{v} = \dot{\boldsymbol{\chi}}$ and $\mathbf{L} = \operatorname{grad}\mathbf{v} = \dot{\mathbf{F}}\mathbf{F}^{-1}$, respectively. In light of these definitions and the multiplicative decomposition of $\mathbf{F}$, we have that

$$\mathbf{L} = \mathbf{L}^{\mathrm{e}} + \mathbf{F}^{\mathrm{e}}\mathbf{L}^{\mathrm{p}}\mathbf{F}^{\mathrm{e}-1}, \tag{6}$$

with

$$\mathbf{L}^{\mathrm{e}} = \dot{\mathbf{F}}^{\mathrm{e}}\mathbf{F}^{\mathrm{e}-1} \quad \text{and} \quad \mathbf{L}^{\mathrm{p}} = \dot{\mathbf{F}}^{\mathrm{p}}\mathbf{F}^{\mathrm{p}-1} \tag{7}$$

representing the elastic and plastic velocity gradients, respectively. The elastic and plastic stretching and spin tensors are denoted by

$$\begin{aligned} \mathbf{D}^{\mathrm{e}} &= \operatorname{sym}\mathbf{L}^{\mathrm{e}}, \qquad \mathbf{W}^{\mathrm{e}} = \operatorname{skw}\mathbf{L}^{\mathrm{e}}, \\ \mathbf{D}^{\mathrm{p}} &= \operatorname{sym}\mathbf{L}^{\mathrm{p}}, \qquad \mathbf{W}^{\mathrm{p}} = \operatorname{skw}\mathbf{L}^{\mathrm{p}}. \end{aligned} \tag{8}$$

As is standard, we assume plastic flow to be irrotational, $\mathbf{W}^{\mathrm{p}} = \mathbf{0}$ [31]. We also make the assumption that plastic flow proceeds at constant volume, so that $J^{\mathrm{p}} = \det\mathbf{F}^{\mathrm{p}} = 1$, $J = J^{\mathrm{e}}$, and $\operatorname{tr}\mathbf{L}^{\mathrm{p}} = \operatorname{tr}\mathbf{D}^{\mathrm{p}} = 0$. This is a standard assumption in the modeling of steady granular flow [32, 25, 33, 34, 4, 14, 15] and provides considerable simplification. This is equivalent to assuming that the material is always in its "critical state" [35], and all transient plastic volumetric dilatation or compaction (which is an important aspect of granular deformation [36, 37]) has subsided.

Finally, we introduce a non-negative, scalar state parameter g, with units of (1/time), referred to as the granular fluidity, which characterizes the susceptibility of a point in a granular media to flow. As discussed in the introduction, according to the microscopic model of Bocquet [9], the fluidity may be interpreted as the rate of plastic events. However, further elucidating the precise microscopic meaning of the fluidity is still a matter of ongoing research. For our current purpose, as pointed out by Bocquet [9] and explored further in our later work [15], the granular fluidity at the continuum-level functions as a nonlocal, Ginzburg-Landau-type order parameter,[‡] which describes a phase transition between non-flowing ($g = 0$) and flowing ($g > 0$) states. We will revisit this notion shortly when discussing the dynamics of g.

Elastic response: The Cauchy stress is given by[§]

$$\mathbf{T} = J^{-1}\mathbf{R}^{\mathrm{e}}\mathbf{M}^{\mathrm{e}}\mathbf{R}^{\mathrm{e}\top}, \tag{9}$$

where $\mathbf{M}^{\mathrm{e}}$ is the Mandel stress. In our previous work, we found it more convenient to utilize an elastic Gibbs free energy rather than the more familiar Helmholtz free energy. Thus, the Mandel

[‡]The notion of an order-parameter approach for modeling granular flow goes back to Aranson and Tsimring [32].
[§]We include the factor of J^{-1} in (9) – which was not present when small elastic strains were assumed [15] – so as to be strictly correct for large elastic deformations.

Copyright © 0000 John Wiley & Sons, Ltd.
Prepared using nmeauth.cls

DOI: 10.1002/nme

stress is given implicitly through

$$\mathbf{E}^{\mathrm{e}} = -\frac{\partial \phi^{(\mathrm{e})}(\bar{p}, \bar{\tau})}{\partial \mathbf{M}^{\mathrm{e}}}, \tag{10}$$

where $\phi^{(\mathrm{e})}$ is the elastic Gibbs free energy, and

$$\bar{\tau} = \frac{1}{\sqrt{2}} \left| \mathbf{M}_0^{\mathrm{e}} \right|, \quad \bar{p} = -\frac{1}{3} \mathrm{tr} \mathbf{M}^{\mathrm{e}}, \quad \text{and} \quad \mu = \frac{\bar{\tau}}{\bar{p}} \tag{11}$$

are the equivalent shear stress, mean normal pressure, and stress ratio, respectively.

Our concern is in steady granular flows, and since the precise form of the Gibbs free energy and hence the elastic response has little influence on the velocity fields and forces in these situations, we choose a simple quadratic and isotropic form for the free energy $\phi^{(\mathrm{e})}$:

$$\phi^{(\mathrm{e})} = -\frac{1}{2}\frac{\bar{\tau}^2}{S} - \frac{1}{2}\frac{\bar{p}^2}{B}, \tag{12}$$

where $S > 0$ and $B > 0$ are the shear and bulk moduli, respectively. By (10), we have that

$$\mathbf{E}^{\mathrm{e}} = \frac{\mathbf{M}_0^{\mathrm{e}}}{2S} + \frac{\mathrm{tr} \mathbf{M}^{\mathrm{e}}}{9B} \mathbf{1}, \tag{13}$$

which, upon inverting, gives the standard linear relationship between stress and strain

$$\mathbf{M}^{\mathrm{e}} = 2S\mathbf{E}_0^{\mathrm{e}} + B(\mathrm{tr} \mathbf{E}^{\mathrm{e}})\mathbf{1} = \mathbb{C}\left[\mathbf{E}^{\mathrm{e}}\right], \tag{14}$$

where $\mathbb{C} = 2S[\mathbb{I} - (1/3)\mathbf{1} \otimes \mathbf{1}] + B\mathbf{1} \otimes \mathbf{1}$ is the fourth-order elasticity tensor and $\mathbb{I}$ is the fourth-order identity tensor. Denoting the spatial Hencky elastic strain as

$$\bar{\mathbf{E}}^{\mathrm{e}} = \mathbf{R}^{\mathrm{e}} \mathbf{E}^{\mathrm{e}} \mathbf{R}^{\mathrm{e}\mathsf{T}} = \ln \mathbf{V}^{\mathrm{e}}, \tag{15}$$

the elastic stress-strain relation may be expressed spatially as

$$\mathbf{T}_{\mathrm{K}} = J\mathbf{T} = 2S\bar{\mathbf{E}}_0^{\mathrm{e}} + B(\mathrm{tr} \bar{\mathbf{E}}^{\mathrm{e}})\mathbf{1} = \mathbb{C}[\bar{\mathbf{E}}^{\mathrm{e}}], \tag{16}$$

where $\mathbf{T}_{\mathrm{K}}$ is the Kirchhoff stress.

Plastic response: The evolution of $\mathbf{F}^{\mathrm{p}}$ is given by

$$\dot{\mathbf{F}}^{\mathrm{p}} = \mathbf{D}^{\mathrm{p}} \mathbf{F}^{\mathrm{p}}, \tag{17}$$

with $\mathbf{D}^{\mathrm{p}}$ given by

$$\mathbf{D}^{\mathrm{p}} = \frac{1}{2} \left(\frac{g}{\bar{p}} \right) \mathbf{M}_0^{\mathrm{e}}, \tag{18}$$

where we have made the common assumption of codirectionality [3, 38, 4, 14, 15] of the plastic stretching and Mandel stress tensors. Defining the equivalent shear plastic strain rate as

$$\dot{\gamma}^{\mathrm{p}} = \sqrt{2} \left| \mathbf{D}^{\mathrm{p}} \right| \tag{19}$$

and utilizing the definitions (11), (18) implies that

$$\dot{\gamma}^{\mathrm{p}} = g\mu. \tag{20}$$

Hence, the tensorial constitutive relation (18) implies the scalar constitutive relation involving g introduced in (2).

Copyright © 0000 John Wiley & Sons, Ltd.
Prepared using nmeauth.cls

DOI: 10.1002/nme

Nonlocal rheology and fluidity boundary conditions: In a conventional local approach, the fluidity would be given constitutively as an algebraic function of the stress through μ and $\bar{p}$. For the local inertial rheology, $g_{\rm loc}(\mu,\bar{p}) = \dot{\gamma}^{\rm P}_{\rm loc}(\mu,\bar{p})/\mu$ with $\dot{\gamma}^{\rm P}_{\rm loc}(\mu,\bar{p})$ given through a relation such as (1). In contrast, in our nonlocal approach, a differential equation involving spatial derivatives of g relates the fluidity to the stress. As derived in our previous work [15], this differential relation follows from a microforce balance – based on the approach of Gurtin [39] – which after further specialization, results in the following primitive, dynamical form for the partial differential equation (PDE) for the fluidity

$$t_0\dot{g} = A^2 d^2 \nabla^2 g - (\mu_{\rm s} - \mu)g - b\sqrt{\frac{\rho_{\rm s} d^2}{\bar{p}}}\mu g^2, \tag{21}$$

where the operator $\nabla^2(\cdot) = \mathrm{div}\,(\mathrm{grad}\,(\cdot))$ represents the *spatial* Laplacian operator. Here, t_0 is a constant time-scale associated with the dynamics of g, A is a dimensionless material parameter characterizing nonlocal effects called the nonlocal amplitude, and the dimensionless constants $\mu_{\rm s}$ and b will shortly be shown to play a similar role as in (1). The mean grain diameter and grain material density continue to be denoted by d and $\rho_{\rm s}$, respectively. This structure of PDE is common to Ginzburg-Landau analysis and makes clear the role of the granular fluidity g as an order parameter. The term on the left-hand side of (21) represents non-steady effects associated with the evolution of g, the first term on the right-hand side accounts for nonlocal effects, and the final two terms are given through the derivative of a "coarse-grain" free energy – a common component in Ginzburg-Landau analysis.

In practice, we are concerned with steady granular flows; however, reducing (21) to the steady-state case is not as simple as setting the left-hand side to zero, since the stability of g-solutions depends on the sign of $(\mu_{\rm s} - \mu)$. Denoting the steady solution of (21) in the absence of spatial gradients as $g_{\rm loc}$, for $\mu < \mu_{\rm s}$, the stable solution is $g_{\rm loc} = 0$, while for $\mu > \mu_{\rm s}$, the stable solution is $g_{\rm loc} = \sqrt{\bar{p}/\rho_{\rm s} d}(\mu - \mu_{\rm s})/(b\mu)$. Hence, as $(\mu_{\rm s} - \mu)$ changes signs, (21) describes a second-order phase transition from non-flowing to flowing states. Putting these together, we recover the local rheology

$$g_{\rm loc}(\bar{p},\mu) = \begin{cases} \sqrt{\bar{p}/\rho_{\rm s} d^2}\,(\mu - \mu_{\rm s})\,/(b\mu) & \text{if } \mu > \mu_{\rm s}, \\ 0 & \text{if } \mu \le \mu_{\rm s}. \end{cases} \tag{22}$$

Finally, in order to obtain a differential relation for g specialized to the case of steady flow, we allow for gradients in g but limit attention to small deviations of g from $g_{\rm loc}$ – a calculation detailed in [15]. The result is the following nonlocal differential relation for the granular fluidity:

$$\nabla^2 g = \frac{1}{\xi^2}(g - g_{\rm loc}) \text{ in } \mathcal{B}_t \tag{23}$$

where $g_{\rm loc}$ is the local fluidity of (22) and ξ is the cooperativity length. Importantly, this analysis gives that the cooperativity length is not constant but depends upon stress as follows,

$$\xi(\mu) = \frac{Ad}{\sqrt{|\mu - \mu_{\rm s}|}}. \tag{24}$$

Hence, the critical parameter $\mu_{\rm s}$ represents both the value of μ at which yield occurs in homogeneous simple shear and the value of μ at which the cooperativity length diverges. This notion that the cooperativity length diverges at the yield point is not unusual and is consistent with past works on length-scale effects in amorphous materials [8, 40, 41, 42]. Finally, it bears noting that the dimensionless parameter A appearing in (24) is the only new material parameter beyond the local parameters introduced in the nonlocal model. Recent work has shown that A is influenced by the properties of the grains themselves, such as the inter-granular friction coefficient [43]

To specify boundary conditions for the differential relation (23), we introduce a set of complementary subsurfaces $\mathcal{S}_g$ and $\mathcal{S}_\zeta$ ($\mathcal{S}_g \cup \mathcal{S}_\zeta = \partial\mathcal{B}_t, \mathcal{S}_g \cap \mathcal{S}_\zeta = \varnothing$) on which the granular fluidity and the normal component of its gradient are prescribed, respectively. The fluidity boundary

Copyright © 0000 John Wiley & Sons, Ltd.
Prepared using nmeauth.cls

DOI: 10.1002/nme

conditions on $\partial\mathcal{B}_t$ are then given by

$$g = \breve{g} \text{ on } \mathcal{S}_g \quad \text{and} \quad \operatorname{grad} g \cdot \mathbf{n} = \breve{\zeta} \text{ on } \mathcal{S}_\zeta, \tag{25}$$

where $\breve{g}$ and $\breve{\zeta}$ are prescribed. Based on our previous work [15], the quantity $\breve{\zeta}$ may be interpreted as a microscopic traction that expends power conjugate to $\dot{g}$ on the boundary $\partial\mathcal{B}_t$.

Equilibrium and mechanical boundary conditions: Finally, the governing partial differential equations are completed by the equations of equilibrium,

$$\operatorname{div} \mathbf{T} + \mathbf{b}_0 = \mathbf{0} \text{ in } \mathcal{B}_t \tag{26}$$

with $\mathbf{T}$ given by (9), $\mathbf{b}_0$ the non-inertial body force per unit volume, and we have neglected macroscopic inertia. Typically, the body force is due to gravity, so that

$$\mathbf{b}_0 = \phi \rho_{\mathrm{s}} \mathbf{G}, \tag{27}$$

where ϕ is the solid volume fraction (for random close packing of quasi-monodisperse spherical grains, $\phi \approx 0.62$), and $\mathbf{G}$ is the acceleration of gravity vector. We denote the acceleration of gravity with a capital $\mathbf{G}$ (and its magnitude as G) so as to clearly differentiate it from the granular fluidity g.

As before, to specify mechanical boundary conditions, we let $\mathcal{S}_{\mathbf{u}}$ and $\mathcal{S}_{\mathbf{t}}$ denote complementary subsurfaces of the boundary $\partial\mathcal{B}_t$ of the deformed body $\mathcal{B}_t$ ($\mathcal{S}_{\mathbf{u}} \cup \mathcal{S}_{\mathbf{t}} = \partial\mathcal{B}_t$, $\mathcal{S}_{\mathbf{u}} \cap \mathcal{S}_{\mathbf{t}} = \varnothing$) where displacements and surface tractions are prescribed, respectively. With $\mathbf{u}(\mathbf{X}, t) = \boldsymbol{\chi}(\mathbf{X}, t) - \mathbf{X}$ denoting the displacement field, the mechanical boundary conditions on $\partial\mathcal{B}_t$ are given by

$$\mathbf{u} = \breve{\mathbf{u}} \text{ on } \mathcal{S}_{\mathbf{u}} \quad \text{and} \quad \mathbf{T}\mathbf{n} = \breve{\mathbf{t}} \text{ on } \mathcal{S}_{\mathbf{t}}, \tag{28}$$

where $\breve{\mathbf{u}}$ and $\breve{\mathbf{t}}$ are prescribed.

3. FINITE-ELEMENT IMPLEMENTATION

Weak form of the governing equations: The set of equations (22), (23), (24), and (26), together with the boundary conditions (25) and (28), represent the strong form of a boundary-value problem for the displacements $\mathbf{u}$ and the granular fluidity g. Our finite-element formulation is based upon the weak form of the governing equations. We introduce two weighting (or test) fields $\boldsymbol{\varphi}$ and ϖ that vanish on $\mathcal{S}_{\mathbf{u}}$ and $\mathcal{S}_g$, respectively, and write the corresponding weak forms of (22)-(28) as

$$\begin{aligned} &\int_{\mathcal{B}_t} \left(\mathbf{T} : \frac{\partial \boldsymbol{\varphi}}{\partial \mathbf{x}} - \boldsymbol{\varphi} \cdot \mathbf{b}_0 \right) dv = \int_{\mathcal{S}_{\mathbf{t}}} \left(\boldsymbol{\varphi} \cdot \breve{\mathbf{t}} \right) da, \\ &\int_{\mathcal{B}_t} \left[\frac{\partial g}{\partial \mathbf{x}} \cdot \frac{\partial \varpi}{\partial \mathbf{x}} + \varpi \left(\frac{g - g_{\mathrm{loc}}}{\xi^2} \right) \right] dv = \int_{\mathcal{S}_\zeta} \left(\varpi \breve{\zeta} \right) da. \end{aligned} \tag{29}$$

We require that trial solutions, $\mathbf{u}$ and g, satisfy the boundary conditions $\mathbf{u} = \breve{\mathbf{u}}$ on $\mathcal{S}_{\mathbf{u}}$ and $g = \breve{g}$ on $\mathcal{S}_g$ and that $\mathbf{u}$ and g and each component of their gradients be square-integrable in the domain $\mathcal{B}_t$, so that the set of trial solutions is denoted as

$$\begin{aligned} \mathbb{S}_{\mathbf{u}} &= \{ \mathbf{u} | \mathbf{u} \in [H^1(\mathcal{B}_t)]^3, \mathbf{u} = \breve{\mathbf{u}} \text{ on } \mathcal{S}_{\mathbf{u}} \}, \\ \mathbb{S}_g &= \{ g | g \in H^1(\mathcal{B}_t), g = \breve{g} \text{ on } \mathcal{S}_g \}, \end{aligned} \tag{30}$$

where H^1 denotes the Sobolev space of degree one. The sets of weighting fields, $\boldsymbol{\varphi}$ and ϖ, are similar to the trial solutions, except that they must vanish on the portions of the boundary $\mathcal{S}_{\mathbf{u}}$ and $\mathcal{S}_g$, respectively, i.e.,

$$\begin{aligned} \mathbb{V}_{\boldsymbol{\varphi}} &= \{ \boldsymbol{\varphi} | \boldsymbol{\varphi} \in [H^1(\mathcal{B}_t)]^3, \boldsymbol{\varphi} = \mathbf{0} \text{ on } \mathcal{S}_{\mathbf{u}} \}, \\ \mathbb{V}_{\varpi} &= \{ \varpi | \varpi \in H^1(\mathcal{B}_t), \varpi = 0 \text{ on } \mathcal{S}_g \}. \end{aligned} \tag{31}$$

Copyright © 0000 John Wiley & Sons, Ltd.

Prepared using nmeauth.cls
DOI: 10.1002/nme

Finite-element discretization and residuals: Based on the structure of the weak form of the boundary-value problem (29), we undertake a two-field ($\mathbf{u}$-g) finite-element formulation. This approach of interpolating the displacement field along with another scalar field has a long tradition in nonlocal and multi-physics problems in mechanics, which we draw upon in developing our formulation. Examples include thermo-mechanically-coupled problems (displacement and temperature); poromechanics problems (displacement and pore fluid pressure) [44, 45]; chemo-mechanically-coupled problems (displacement and chemical potential) [46]; electro-mechanically-coupled problems (displacement and electric field) [47, 48]; phase-field modeling of brittle fracture (displacement and a scalar phase-field damage variable) [49, 50]; and both implicit and explicit gradient plasticity (displacement and a scalar plastic strain or strain-like variable) [18, 22]; among others.

The body is spatially discretized using finite elements, $\mathcal{B}_t = \cup \mathcal{B}^{\mathrm{e}}$, and the functional sets $\mathbb{S}_{\mathbf{u}}$, $\mathbb{S}_g$, $\mathbb{V}_{\boldsymbol{\varphi}}$, and $\mathbb{V}_{\varpi}$ are replaced with finite-dimensional subsets, $\mathbb{S}^h_{\mathbf{u}}$, $\mathbb{S}^h_g$, $\mathbb{V}^h_{\boldsymbol{\varphi}}$, and $\mathbb{V}^h_{\varpi}$, generated through the discretization of $\mathcal{B}_t$. Here, the index h denotes the characteristic mesh size of the finite-element discretization. Denoting the number of nodes in a generic finite element $\mathcal{B}^{\mathrm{e}}$ by n, the finite-element approximations, $\mathbf{u}^h$ and g^h, of the displacement and granular fluidity fields, $\mathbf{u}$ and g, inside the element $\mathcal{B}^{\mathrm{e}}$ are given by

$$\mathbf{u}^h = \sum_{A=1}^{n} \mathbf{u}^A N^A \quad \text{and} \quad g^h = \sum_{A=1}^{n} g^A N^A \tag{32}$$

with the index $A = 1, 2, \ldots$ denoting the nodes of the element, $\mathbf{u}^A$ and g^A the nodal displacements and fluidities, and N^A the element shape functions, or interpolating functions. We emphasize that the *same* shape functions are used to interpolate both the displacement and granular fluidity fields. We then employ a standard Galerkin approach, in that the weighting fields, $\boldsymbol{\varphi}$ and ϖ, are interpolated by the same shape functions,

$$\boldsymbol{\varphi}^h = \sum_{A=1}^{n} \boldsymbol{\varphi}^A N^A \quad \text{and} \quad \varpi^h = \sum_{A=1}^{n} \varpi^A N^A \quad \text{in} \quad \mathcal{B}^{\mathrm{e}}. \tag{33}$$

Again, the same shape functions are used to interpolate both weighting fields. Using (32) and (33) in (29) yields the following element-level system of equations,

$$\begin{aligned} \int_{\mathcal{B}^{\mathrm{e}}} \left(\mathbf{T} \frac{\partial N^A}{\partial \mathbf{x}} - N^A \mathbf{b}_0 \right) dv &= \int_{\mathcal{S}^{\mathrm{e}}_{\mathbf{t}}} \left(N^A \check{\mathbf{t}} \right) da, \\ \int_{\mathcal{B}^{\mathrm{e}}} \left[\frac{\partial g}{\partial \mathbf{x}} \cdot \frac{\partial N^A}{\partial \mathbf{x}} + N^A \left(\frac{g - g_{\mathrm{loc}}}{\xi^2} \right) \right] dv &= \int_{\mathcal{S}^{\mathrm{e}}_{\zeta}} \left(N^A \check{\zeta} \right) da, \end{aligned} \tag{34}$$

which may then be used to define the following element-level residuals for the displacement and granular fluidity

$$\begin{aligned} (\mathbf{R}_{\mathbf{u}})^A &= -\int_{\mathcal{B}^{\mathrm{e}}} \left(\mathbf{T} \frac{\partial N^A}{\partial \mathbf{x}} - N^A \mathbf{b}_0 \right) dv + \int_{\mathcal{S}^{\mathrm{e}}_{\mathbf{t}}} \left(N^A \check{\mathbf{t}} \right) da, \\ (\mathbf{R}_g)^A &= \int_{\mathcal{B}^{\mathrm{e}}} \left[\frac{\partial g}{\partial \mathbf{x}} \cdot \frac{\partial N^A}{\partial \mathbf{x}} + N^A \left(\frac{g - g_{\mathrm{loc}}}{\xi^2} \right) \right] dv - \int_{\mathcal{S}^{\mathrm{e}}_{\zeta}} \left(N^A \check{\zeta} \right) da. \end{aligned} \tag{35}$$

Since nodes, and hence nodal degrees of freedom, can take part in multiple elements, the element-level residuals are assembled into a set of global residuals, which when set equal to zero, represent a non-linear system of equations for the nodal degrees of freedom, which may be solved iteratively using a Newton-Raphson procedure.

Temporal discretization: Calculation of the element-level residuals (35) requires the quantities $\mathbf{T}$, g_{loc}, and ξ. Since our constitutive equations are history-dependent (due to the evolution equation

Copyright © 0000 John Wiley & Sons, Ltd.
Prepared using nmeauth.cls

DOI: 10.1002/nme

(17)), a numerical algorithm for the time-integration of the constitutive equations is required. In the incremental, time-discrete form of the constitutive theory, it is assumed that at some time t_{n}, the state of the material, i.e., $\mathbf{F}^{\mathrm{p}}_{\mathrm{n}}$, is known. Then, given $\mathbf{F}_{\mathrm{n+1}}$ and $g_{\mathrm{n+1}}$ at time $t_{\mathrm{n+1}} = t_{\mathrm{n}} + \Delta t$, the Cauchy stress, local fluidity, and cooperativity length at time $t_{\mathrm{n+1}}$ are to be determined through the time-integration procedure. The derivation of such a procedure is non-trivial, and details are given in Section 4. Of course, the time-integration procedure should be accompanied by initial conditions. Throughout, we assume that at time $t = 0$,

$$\mathbf{F}(\mathbf{X}, t = 0) = \mathbf{F}^{\mathrm{p}}(\mathbf{X}, t = 0) = \mathbf{1} \quad \text{and} \quad g(\mathbf{X}, t = 0) = 0. \tag{36}$$

Tangents: In order to complete an iteration of the Newton-Raphson procedure, tangent moduli, determined by linearizing the residuals about a given state, are required. Element-level tangents corresponding to the residuals (35) are defined by

$$\begin{aligned} \mathbf{K}^{AB}_{\mathbf{uu}} &= -\frac{\partial \mathbf{R}^{A}_{\mathbf{u}}}{\partial \mathbf{u}^{B}}, \quad \mathbf{K}^{AB}_{\mathbf{u}g} = -\frac{\partial \mathbf{R}^{A}_{\mathbf{u}}}{\partial g^{B}}, \\ \mathbf{K}^{AB}_{g\mathbf{u}} &= -\frac{\partial \mathbf{R}^{A}_{g}}{\partial \mathbf{u}^{B}}, \quad \mathbf{K}^{AB}_{gg} = -\frac{\partial \mathbf{R}^{A}_{g}}{\partial g^{B}}. \end{aligned} \tag{37}$$

Like the residuals, the element-level tangents are then assembled into a set of global tangents. Importantly, in order to obtain ideal performance of the Newton-Raphson procedure, the tangents should be calculated using the time-discrete form of the constitutive theory, i.e., they should be algorithmically-consistent. Details of the derivation of algorithmically-consistent tangents are given in Section 5.

Specifics of the implementation: In order to make our implementation portable and widely available to the broad research community working on granular flow, the finite-element procedures have been implemented in Abaqus/Standard [27], using a user-element subroutine (UEL). During an analysis, the user subroutine UEL is called for each Newton-Raphson iteration in a given time increment. The initial nodal coordinates; the coordinates, granular fluidities, and internal variables ($\mathbf{F}^{\mathrm{p}}$) from the previous converged increment (at time $t = t_{\mathrm{n}}$); and the current guesses of the nodal displacements and fluidities (at time $t = t_{\mathrm{n+1}}$) are passed into the subroutine, and the element-level residuals (35), consistent tangents (37), and updated internal variables are required as outputs.

Regarding the specific shape functions N^A used in our implementation, since the boundary-value problem is elliptic in nature and no second gradients of the displacement or granular fluidity fields appear in the residuals (35), we are able to use simple, piecewise linear shape functions with C^0 continuity. That is to say, piecewise linear, C^0 functions belong to the functional sets (30) and (31). (Recall that we use the same shape functions to interpolate both the displacement and granular fluidity fields.) We have developed two types of linear, C^0, isoparametric finite elements:

1. A three-dimensional (3D), eight-noded continuum brick user element. The nodal degrees of freedom of the 3D element are the three components of displacement, u_x, u_y, and u_z, along with the granular fluidity g, which are interpolated over the three dimensions, x, y, and z.
2. A two-dimensional, four-noded generalized axisymmetric (GAX) element. The nodal degrees of freedom of the GAX element are the radial and vertical displacements, u_r and u_z, the angle of rotation θ, and the granular fluidity g, which are interpolated over two dimensions, r and z.

We have made our two Abaqus user-element subroutines available online as supporting information.

Volumetric locking: Finally, in order to avoid issues related to volumetric-locking, we utilize the F-bar method of de Souza Neto et al for fully integrated elements [51, 52]. In short, in this method, the deformation gradient is modified so that volumetric deformation – and hence the pressure – is constant inside of an element. Once this modification is made, the residuals and tangents may be fully-integrated without volumetric locking. This approach has the benefit that no modification is

Copyright © 0000 John Wiley & Sons, Ltd.
Prepared using nmeauth.cls

DOI: 10.1002/nme

needed in calculating the integration-point residuals. However, slight, straightforward modifications are needed in calculating the tangents $\mathbf{K}^{AB}_{\mathbf{uu}}$ and $\mathbf{K}^{AB}_{g\mathbf{u}}$. For further details on this point and on implementing user element subroutines in Abaqus in general, see the work of Chester et al [46].

4. TIME-INTEGRATION PROCEDURE

In this section, we derive an implicit time integration procedure for the constitutive theory of Section 2. Given $\mathbf{F}^{\mathrm{p}}_{\mathrm{n}}$ at time t_{n} as well as $\mathbf{F}_{\mathrm{n+1}}$ and $g_{\mathrm{n+1}}$ at time $t_{\mathrm{n+1}} = t_{\mathrm{n}} + \Delta t$, we are to calculate the Cauchy stress $\mathbf{T}_{\mathrm{n+1}}$ and the plastic deformation gradient $\mathbf{F}^{\mathrm{p}}_{\mathrm{n+1}}$ as well as the cooperativity length $\xi_{\mathrm{n+1}}$ and local fluidity $g^{\mathrm{loc}}_{\mathrm{n+1}}$.¶

We begin by integrating the evolution equation for $\mathbf{F}^{\mathrm{p}}$ (17) via the exponential map [53, 52]

$$\mathbf{F}^{\mathrm{p}}_{\mathrm{n+1}} = \exp\left(\Delta t\, \mathbf{D}^{\mathrm{p}}_{\mathrm{n+1}}\right) \mathbf{F}^{\mathrm{p}}_{\mathrm{n}}, \quad \text{with} \quad \mathbf{D}^{\mathrm{p}}_{\mathrm{n+1}} = \hat{\mathbf{D}}^{\mathrm{p}}_{\mathrm{n+1}}(\mathbf{M}^{\mathrm{e}}_{\mathrm{n+1}}, g_{\mathrm{n+1}}). \tag{38}$$

With the inverse of $\mathbf{F}^{\mathrm{p}}_{\mathrm{n+1}}$ given by

$$\mathbf{F}^{\mathrm{p}-1}_{\mathrm{n+1}} = \mathbf{F}^{\mathrm{p}-1}_{\mathrm{n}} \exp\left(-\Delta t\, \mathbf{D}^{\mathrm{p}}_{\mathrm{n+1}}\right) \tag{39}$$

and

$$\mathbf{F}^{\mathrm{e}}_{\mathrm{n+1}} = \mathbf{F}_{\mathrm{n+1}} \mathbf{F}^{\mathrm{p}-1}_{\mathrm{n+1}}, \tag{40}$$

we have that the elastic deformation gradient at the end of the step is

$$\mathbf{F}^{\mathrm{e}}_{\mathrm{n+1}} = \mathbf{F}^{\mathrm{e}}_{\mathrm{tr}} \exp\left(-\Delta t\, \mathbf{D}^{\mathrm{p}}_{\mathrm{n+1}}\right), \tag{41}$$

where

$$\mathbf{F}^{\mathrm{e}}_{\mathrm{tr}} = \mathbf{F}_{\mathrm{n+1}} \mathbf{F}^{\mathrm{p}-1}_{\mathrm{n}} \tag{42}$$

is a trial value of $\mathbf{F}^{\mathrm{e}}$. Trial values correspond to the value of a quantity at the end of the step when plastic flow is frozen.

The tensors $\mathbf{F}^{\mathrm{e}}_{\mathrm{n+1}}$ and $\mathbf{F}^{\mathrm{e}}_{\mathrm{tr}}$ admit the polar decompositions

$$\mathbf{F}^{\mathrm{e}}_{\mathrm{n+1}} = \mathbf{R}^{\mathrm{e}}_{\mathrm{n+1}} \mathbf{U}^{\mathrm{e}}_{\mathrm{n+1}} \quad \text{and} \quad \mathbf{F}^{\mathrm{e}}_{\mathrm{tr}} = \mathbf{R}^{\mathrm{e}}_{\mathrm{tr}} \mathbf{U}^{\mathrm{e}}_{\mathrm{tr}}, \tag{43}$$

respectively, so that, upon rearranging, (41) may be written as

$$\mathbf{R}^{\mathrm{e}}_{\mathrm{n+1}} \mathbf{U}^{\mathrm{e}}_{\mathrm{n+1}} \exp\left(\Delta t\, \mathbf{D}^{\mathrm{p}}_{\mathrm{n+1}}\right) = \mathbf{R}^{\mathrm{e}}_{\mathrm{tr}} \mathbf{U}^{\mathrm{e}}_{\mathrm{tr}}, \tag{44}$$

Due to the isotropic constitutive equation $(38)_2$, the tensors $\mathbf{D}^{\mathrm{p}}_{\mathrm{n+1}}$ and $\mathbf{M}^{\mathrm{e}}_{\mathrm{n+1}}$ have the same principal directions. Similarly, due to the constitutive equation (14), $\mathbf{M}^{\mathrm{e}}_{\mathrm{n+1}}$ and $\mathbf{E}^{\mathrm{e}}_{\mathrm{n+1}}$, and hence $\mathbf{U}^{\mathrm{e}}_{\mathrm{n+1}}$, also share principal directions. Therefore, the tenors $\mathbf{D}^{\mathrm{p}}_{\mathrm{n+1}}$ and $\mathbf{U}^{\mathrm{e}}_{\mathrm{n+1}}$ have the same principal directions, and the tensor $\mathbf{U}^{\mathrm{e}}_{\mathrm{n+1}} \exp\left(\Delta t\, \mathbf{D}^{\mathrm{p}}_{\mathrm{n+1}}\right)$ is symmetric. Due to the uniqueness of the polar decomposition, this leads us to conclude that

$$\begin{aligned} \mathbf{R}^{\mathrm{e}}_{\mathrm{n+1}} &= \mathbf{R}^{\mathrm{e}}_{\mathrm{tr}}, \\ \mathbf{U}^{\mathrm{e}}_{\mathrm{n+1}} &= \mathbf{U}^{\mathrm{e}}_{\mathrm{tr}} \exp\left(-\Delta t\, \mathbf{D}^{\mathrm{p}}_{\mathrm{n+1}}\right). \end{aligned} \tag{45}$$

By $(45)_2$, $\mathbf{U}^{\mathrm{e}}_{\mathrm{n+1}}$ and $\mathbf{U}^{\mathrm{e}}_{\mathrm{tr}}$ share principal directions, and consequently, upon taking the logarithm of $(45)_2$, we obtain the following update equation for the Hencky strain:

$$\mathbf{E}^{\mathrm{e}}_{\mathrm{n+1}} = \mathbf{E}^{\mathrm{e}}_{\mathrm{tr}} - \Delta t\, \mathbf{D}^{\mathrm{p}}_{\mathrm{n+1}} \quad \text{with} \quad \mathbf{E}^{\mathrm{e}}_{\mathrm{tr}} = \ln \mathbf{U}^{\mathrm{e}}_{\mathrm{tr}}. \tag{46}$$

¶To avoid overly lengthy subscripts, we denote the local fluidity as g^{loc} when discussing the time-integration procedure. Similarly, the Kirchhoff stress will be denoted as $\mathbf{T}^{\mathrm{K}}$ in the subsequent section.

Copyright © 0000 John Wiley & Sons, Ltd.

Prepared using nmeauth.cls
DOI: 10.1002/nme

Further, utilizing the stress-strain relation (14), we obtain

$$\mathbf{M}^{\mathrm{e}}_{\mathrm{n+1}} = \mathbf{M}^{\mathrm{e}}_{\mathrm{tr}} - 2S\Delta t\, \mathbf{D}^{\mathrm{p}}_{\mathrm{n+1}} \quad \text{with} \quad \mathbf{M}^{\mathrm{e}}_{\mathrm{tr}} = \mathbb{C}[\mathbf{E}^{\mathrm{e}}_{\mathrm{tr}}] \tag{47}$$

and we have made use of the deviatoric nature of $\mathbf{D}^{\mathrm{p}}_{\mathrm{n+1}}$.

Next, we write

$$\mathbf{D}^{\mathrm{p}}_{\mathrm{n+1}} = \frac{1}{\sqrt{2}}\dot{\gamma}^{\mathrm{p}}_{\mathrm{n+1}}\mathbf{N}^{\mathrm{p}}_{\mathrm{n+1}}, \tag{48}$$

where $\dot{\gamma}^{\mathrm{p}}_{\mathrm{n+1}} = \sqrt{2}|\mathbf{D}^{\mathrm{p}}_{\mathrm{n+1}}|$ is the equivalent shear plastic strain rate and $\mathbf{N}^{\mathrm{p}}_{\mathrm{n+1}} = \mathbf{D}^{\mathrm{p}}_{\mathrm{n+1}}/|\mathbf{D}^{\mathrm{p}}_{\mathrm{n+1}}|$ is the symmetric and deviatoric direction of plastic flow. From (18),

$$\dot{\gamma}^{\mathrm{p}}_{\mathrm{n+1}} = g_{\mathrm{n+1}}\mu_{\mathrm{n+1}} \quad \text{and} \quad \mathbf{N}^{\mathrm{p}}_{\mathrm{n+1}} = \frac{\mathbf{M}^{\mathrm{e}}_{0,\mathrm{n+1}}}{\sqrt{2}\bar{\tau}_{\mathrm{n+1}}}, \tag{49}$$

where

$$\bar{\tau}_{\mathrm{n+1}} = \frac{1}{\sqrt{2}}\left|\mathbf{M}^{\mathrm{e}}_{0,\mathrm{n+1}}\right|, \quad \bar{p}_{\mathrm{n+1}} = -\frac{1}{3}\mathrm{tr}\mathbf{M}^{\mathrm{e}}_{\mathrm{n+1}}, \quad \text{and} \quad \mu_{\mathrm{n+1}} = \frac{\bar{\tau}_{\mathrm{n+1}}}{\bar{p}_{\mathrm{n+1}}}. \tag{50}$$

Using (48) in (47), we have

$$\mathbf{M}^{\mathrm{e}}_{\mathrm{n+1}} = \mathbf{M}^{\mathrm{e}}_{\mathrm{tr}} - \sqrt{2}S(\Delta t\dot{\gamma}^{\mathrm{p}}_{\mathrm{n+1}})\mathbf{N}^{\mathrm{p}}_{\mathrm{n+1}}. \tag{51}$$

Splitting (51) into deviatoric and spherical parts, we may conclude

$$\begin{aligned} &\mathbf{M}^{\mathrm{e}}_{0,\mathrm{n+1}} = \mathbf{M}^{\mathrm{e}}_{0,\mathrm{tr}} - \sqrt{2}S(\Delta t\dot{\gamma}^{\mathrm{p}}_{\mathrm{n+1}})\mathbf{N}^{\mathrm{p}}_{\mathrm{n+1}}, \\ &\bar{p}_{\mathrm{n+1}} = \bar{p}_{\mathrm{tr}}, \end{aligned} \tag{52}$$

where $\bar{p}_{\mathrm{tr}} = -(1/3)\mathrm{tr}\mathbf{M}^{\mathrm{e}}_{\mathrm{tr}}$ is the trial pressure. Further, defining the trial equivalent shear stress and trial direction of plastic flow as

$$\bar{\tau}_{\mathrm{tr}} = \frac{1}{\sqrt{2}}\left|\mathbf{M}^{\mathrm{e}}_{0,\mathrm{tr}}\right| \quad \text{and} \quad \mathbf{N}^{\mathrm{p}}_{\mathrm{tr}} = \frac{\mathbf{M}^{\mathrm{e}}_{0,\mathrm{tr}}}{\sqrt{2}\bar{\tau}_{\mathrm{tr}}}, \tag{53}$$

respectively, and utilizing the definitions (50), we may write $(52)_1$ as

$$\left(\bar{\tau}_{\mathrm{n+1}} + S(\Delta t\dot{\gamma}^{\mathrm{p}}_{\mathrm{n+1}})\right)\mathbf{N}^{\mathrm{p}}_{\mathrm{n+1}} = \bar{\tau}_{\mathrm{tr}}\mathbf{N}^{\mathrm{p}}_{\mathrm{tr}}, \tag{54}$$

leading us to conclude that

$$\begin{aligned} &\bar{\tau}_{\mathrm{n+1}} + S(\Delta t\dot{\gamma}^{\mathrm{p}}_{\mathrm{n+1}}) = \bar{\tau}_{\mathrm{tr}}, \\ &\mathbf{N}^{\mathrm{p}}_{\mathrm{n+1}} = \mathbf{N}^{\mathrm{p}}_{\mathrm{tr}}. \end{aligned} \tag{55}$$

Using $(49)_1$, $(50)_3$, and $(52)_2$ in $(55)_1$ and rearranging, we have

$$\bar{\tau}_{\mathrm{n+1}} = \frac{\bar{\tau}_{\mathrm{tr}}\bar{p}_{\mathrm{tr}}}{\bar{p}_{\mathrm{tr}} + S\Delta t g_{\mathrm{n+1}}}, \tag{56}$$

and using (55) in (51) leads to the following update for the Mandel stress

$$\mathbf{M}^{\mathrm{e}}_{\mathrm{n+1}} = \mathbf{M}^{\mathrm{e}}_{\mathrm{tr}} - \sqrt{2}\left(\bar{\tau}_{\mathrm{tr}} - \bar{\tau}_{\mathrm{n+1}}\right)\mathbf{N}^{\mathrm{p}}_{\mathrm{tr}}. \tag{57}$$

The Cauchy stress is then simply updated as

$$\mathbf{T}_{\mathrm{n+1}} = (\det\mathbf{F}_{\mathrm{n+1}})^{-1}\mathbf{R}^{\mathrm{e}}_{\mathrm{tr}}\mathbf{M}^{\mathrm{e}}_{\mathrm{n+1}}\mathbf{R}^{\mathrm{e}\top}_{\mathrm{tr}}, \tag{58}$$

and the updated equivalent shear plastic strain rate, plastic stretching, and plastic distortion are given by

$$\begin{aligned} &\dot{\gamma}^{\mathrm{p}}_{\mathrm{n+1}} = g_{\mathrm{n+1}}\left(\frac{\bar{\tau}_{\mathrm{n+1}}}{\bar{p}_{\mathrm{tr}}}\right), \\ &\mathbf{D}^{\mathrm{p}}_{\mathrm{n+1}} = \frac{1}{\sqrt{2}}\dot{\gamma}^{\mathrm{p}}_{\mathrm{n+1}}\mathbf{N}^{\mathrm{p}}_{\mathrm{tr}}, \quad \text{and} \\ &\mathbf{F}^{\mathrm{p}}_{\mathrm{n+1}} = \exp\left(\Delta t\mathbf{D}^{\mathrm{p}}_{\mathrm{n+1}}\right)\mathbf{F}^{\mathrm{p}}_{\mathrm{n}}. \end{aligned} \tag{59}$$

Finally, it is straightforward to calculate $g^{\mathrm{loc}}_{\mathrm{n+1}}$ and $\xi_{\mathrm{n+1}}$ through (22) and (24), respectively.

Copyright © 0000 John Wiley & Sons, Ltd.
Prepared using nmeauth.cls

DOI: 10.1002/nme

Summary of the implicit time-integration procedure:

- Given: $\{\mathbf{F}_{\mathrm{n}+1}, g_{\mathrm{n}+1}, \mathbf{F}^{\mathrm{p}}_{\mathrm{n}}\}$ at time t_{n}.
- Calculate: $\{\mathbf{T}_{\mathrm{n}+1}, \mathbf{F}^{\mathrm{p}}_{\mathrm{n}+1}, g^{\mathrm{loc}}_{\mathrm{n}+1}, \xi_{\mathrm{n}+1}\}$ at time $t_{\mathrm{n}+1} = t_{\mathrm{n}} + \Delta t$.

Step 1. Calculate the trial elastic deformation gradient:

$$\mathbf{F}^{\mathrm{e}}_{\mathrm{tr}} = \mathbf{F}_{\mathrm{n}+1}\mathbf{F}^{\mathrm{p}-1}_{\mathrm{n}}. \tag{60}$$

Step 2. Perform the polar decomposition and calculate the trial elastic Hencky strain:

$$\mathbf{F}^{\mathrm{e}}_{\mathrm{tr}} = \mathbf{R}^{\mathrm{e}}_{\mathrm{tr}}\mathbf{U}^{\mathrm{e}}_{\mathrm{tr}} \quad \text{and} \quad \mathbf{E}^{\mathrm{e}}_{\mathrm{tr}} = \ln \mathbf{U}^{\mathrm{e}}_{\mathrm{tr}}. \tag{61}$$

Step 3. Calculate the trial Mandel stress and associated quantities:

$$\mathbf{M}^{\mathrm{e}}_{\mathrm{tr}} = \mathbb{C}[\mathbf{E}^{\mathrm{e}}_{\mathrm{tr}}], \quad \bar{p}_{\mathrm{tr}} = -\frac{1}{3}\mathrm{tr}\mathbf{M}^{\mathrm{e}}_{\mathrm{tr}}, \quad \bar{\tau}_{\mathrm{tr}} = \frac{1}{\sqrt{2}}\left|\mathbf{M}^{\mathrm{e}}_{0,\mathrm{tr}}\right|, \quad \text{and} \quad \mathbf{N}^{\mathrm{p}}_{\mathrm{tr}} = \frac{\mathbf{M}^{\mathrm{e}}_{0,\mathrm{tr}}}{\sqrt{2}\bar{\tau}_{\mathrm{tr}}}. \tag{62}$$

Step 4. Update the stresses:

$$\begin{aligned}
&\bar{\tau}_{\mathrm{n}+1} = \frac{\bar{\tau}_{\mathrm{tr}}\bar{p}_{\mathrm{tr}}}{\bar{p}_{\mathrm{tr}} + S\Delta t g_{\mathrm{n}+1}},\\
&\mu_{\mathrm{n}+1} = \bar{\tau}_{\mathrm{n}+1}/\bar{p}_{\mathrm{tr}},\\
&\mathbf{M}^{\mathrm{e}}_{\mathrm{n}+1} = \mathbf{M}^{\mathrm{e}}_{\mathrm{tr}} - \sqrt{2}\left(\bar{\tau}_{\mathrm{tr}} - \bar{\tau}_{\mathrm{n}+1}\right)\mathbf{N}^{\mathrm{p}}_{\mathrm{tr}}, \quad \text{and}\\
&\mathbf{T}_{\mathrm{n}+1} = (\det \mathbf{F}_{\mathrm{n}+1})^{-1}\mathbf{R}^{\mathrm{e}}_{\mathrm{tr}}\mathbf{M}^{\mathrm{e}}_{\mathrm{n}+1}\mathbf{R}^{\mathrm{e}\mathsf{T}}_{\mathrm{tr}}.
\end{aligned} \tag{63}$$

Step 5. Update the plastic stretching and distortion:

$$\begin{aligned}
&\dot{\gamma}^{\mathrm{p}}_{\mathrm{n}+1} = g_{\mathrm{n}+1}\mu_{\mathrm{n}+1},\\
&\mathbf{D}^{\mathrm{p}}_{\mathrm{n}+1} = \frac{1}{\sqrt{2}}\dot{\gamma}^{\mathrm{p}}_{\mathrm{n}+1}\mathbf{N}^{\mathrm{p}}_{\mathrm{tr}}, \quad \text{and}\\
&\mathbf{F}^{\mathrm{p}}_{\mathrm{n}+1} = \exp\left(\Delta t\mathbf{D}^{\mathrm{p}}_{\mathrm{n}+1}\right)\mathbf{F}^{\mathrm{p}}_{\mathrm{n}}.
\end{aligned} \tag{64}$$

Step 6. Update the local fluidity and cooperativity length:[‖]

$$\begin{aligned}
g^{\mathrm{loc}}_{\mathrm{n}+1} &= \begin{cases} \sqrt{\bar{p}_{\mathrm{tr}}/\rho_{\mathrm{s}}d^2}\left(\mu_{\mathrm{n}+1} - \mu_{\mathrm{s}}\right)/\left(b\mu_{\mathrm{n}+1}\right) & \text{if } \mu_{\mathrm{n}+1} > \mu_{\mathrm{s}},\\ 0 & \text{if } \mu_{\mathrm{n}+1} \le \mu_{\mathrm{s}}, \end{cases}\\
\xi_{\mathrm{n}+1} &= \frac{Ad}{\sqrt{|\mu_{\mathrm{n}+1} - \mu_{\mathrm{s}}|}}.
\end{aligned} \tag{65}$$

5. ALGORITHMICALLY-CONSISTENT TANGENTS

Here we will address the calculation of each of the four sets of tangents in light of our implicit time-integration procedure. We will neglect the terms due to external loads, i.e., the terms involving $\mathbf{b}_0$, $\breve{\mathbf{t}}$, and $\breve{\zeta}$ in (35)

[‖] In order to ensure that our implementation remains robust when $\mu \approx \mu_{\mathrm{s}}$, we place a cap on ξ. We utilize a parabolic functional form for the cap, so that the dependence of ξ on μ remains smooth. In all subsequent calculations, we specify a cap on ξ of $1000d$, and we have ensured that this is a sufficiently high cap value so that our calculation results are independent of this choice. We note that only a very small range of μ-values ($\mu_{\mathrm{s}} \pm 10^{-6}$) are affected by the introduction of the cap.

Copyright © 0000 John Wiley & Sons, Ltd.
Prepared using nmeauth.cls

DOI: 10.1002/nme

The mechanical tangents: We begin by calculating the purely mechanical tangents $\mathbf{K}^{AB}_{\mathbf{uu}}$, which may be expressed in component form as $K^{AB}_{u_iu_k}$ as

$$K^{AB}_{u_iu_k} = \int_{\mathcal{B}^{\mathrm{e}}} \left(\frac{\partial N^A}{\partial x_j} \mathcal{C}_{ijkl} \frac{\partial N^B}{\partial x_l} \right) dv, \tag{66}$$

where

$$\mathcal{C}_{ijkl} = \frac{1}{J} F_{lq} \frac{\partial T^{\mathrm{K}}_{ij}}{\partial F_{kq}} - T_{il}\delta_{jk}. \tag{67}$$

and we have left off the subscript $\mathrm{n}+1$ for brevity. Straightforward application of the chain rule leads to the following expression for $\mathcal{C}_{ijkl}$:

$$\mathcal{C}_{ijkl} = \frac{1}{2J} \mathcal{D}_{ijmn} \mathcal{L}_{mnpq} \mathcal{B}_{pqkl} - T_{il}\delta_{jk}, \tag{68}$$

with

$$\boldsymbol{\mathcal{D}} = \frac{\partial \mathbf{T}^{\mathrm{K}}_{\mathrm{n}+1}}{\partial \bar{\mathbf{E}}^{\mathrm{e}}_{\mathrm{tr}}}, \quad \boldsymbol{\mathcal{L}} = \frac{\partial \ln(\mathbf{B}^{\mathrm{e}}_{\mathrm{tr}})}{\partial \mathbf{B}^{\mathrm{e}}_{\mathrm{tr}}}, \quad \text{and} \quad \mathcal{B}_{ijkl} = \delta_{ik} B^{\mathrm{e}}_{\mathrm{tr},jl} + \delta_{jk} B^{\mathrm{e}}_{\mathrm{tr},il} \tag{69}$$

Details of the above calculations may be found in Section 14.5 of [52]. Hence, it remains to calculate $\boldsymbol{\mathcal{D}}$, the important constitutive contribution to $\boldsymbol{\mathcal{C}}$. Applying $\mathbf{R}^{\mathrm{e}}_{\mathrm{tr}}(\cdot)\mathbf{R}^{\mathrm{e}\top}_{\mathrm{tr}}$ to (57), we have

$$\mathbf{T}^{\mathrm{K}}_{\mathrm{n}+1} = \mathbf{T}^{\mathrm{K}}_{\mathrm{tr}} - \sqrt{2}(\bar{\tau}_{\mathrm{tr}} - \bar{\tau}_{\mathrm{n}+1})\bar{\mathbf{N}}^{\mathrm{p}}_{\mathrm{tr}} \tag{70}$$

with

$$\mathbf{T}^{\mathrm{K}}_{\mathrm{tr}} = \mathbf{R}^{\mathrm{e}}_{\mathrm{tr}} \mathbf{M}^{\mathrm{e}}_{\mathrm{tr}} \mathbf{R}^{\mathrm{e}\top}_{\mathrm{tr}} \quad \text{and} \quad \bar{\mathbf{N}}^{\mathrm{p}}_{\mathrm{tr}} = \mathbf{R}^{\mathrm{e}}_{\mathrm{tr}} \mathbf{N}^{\mathrm{p}}_{\mathrm{tr}} \mathbf{R}^{\mathrm{e}\top}_{\mathrm{tr}} = \frac{\mathbf{T}^{\mathrm{K}}_{0,\mathrm{tr}}}{\left|\mathbf{T}^{\mathrm{K}}_{0,\mathrm{tr}}\right|}. \tag{71}$$

We also note that

$$\bar{\tau}_{\mathrm{n}+1} = \frac{1}{\sqrt{2}} \left|\mathbf{T}^{\mathrm{K}}_{0,\mathrm{n}+1}\right| \quad \text{and} \quad \bar{\tau}_{\mathrm{tr}} = \frac{1}{\sqrt{2}} \left|\mathbf{T}^{\mathrm{K}}_{0,\mathrm{tr}}\right|. \tag{72}$$

Next, applying the chain rule to (70), we obtain

$$\boldsymbol{\mathcal{D}} = \frac{\partial \mathbf{T}^{\mathrm{K}}_{\mathrm{tr}}}{\partial \bar{\mathbf{E}}^{\mathrm{e}}_{\mathrm{tr}}} + \sqrt{2}(\bar{\tau}_{\mathrm{n}+1} - \bar{\tau}_{\mathrm{tr}}) \frac{\partial \bar{\mathbf{N}}^{\mathrm{p}}_{\mathrm{tr}}}{\partial \bar{\mathbf{E}}^{\mathrm{e}}_{\mathrm{tr}}} + \bar{\mathbf{N}}^{\mathrm{p}}_{\mathrm{tr}} \otimes \left[\sqrt{2} \left(\frac{\partial \bar{\tau}_{\mathrm{n}+1}}{\partial \bar{\mathbf{E}}^{\mathrm{e}}_{\mathrm{tr}}} - \frac{\partial \bar{\tau}_{\mathrm{tr}}}{\partial \bar{\mathbf{E}}^{\mathrm{e}}_{\mathrm{tr}}} \right) \right]. \tag{73}$$

Since $\mathbf{T}^{\mathrm{K}}_{\mathrm{tr}} = \mathbb{C}[\bar{\mathbf{E}}^{\mathrm{e}}_{\mathrm{tr}}]$, we have

$$\frac{\partial \mathbf{T}^{\mathrm{K}}_{\mathrm{tr}}}{\partial \bar{\mathbf{E}}^{\mathrm{e}}_{\mathrm{tr}}} = \mathbb{C} \quad \text{and} \quad \frac{\partial \mathbf{T}^{\mathrm{K}}_{0,\mathrm{tr}}}{\partial \bar{\mathbf{E}}^{\mathrm{e}}_{\mathrm{tr}}} = 2S \left(\mathbb{I} - \frac{1}{3} \mathbf{1} \otimes \mathbf{1} \right). \tag{74}$$

Next, using the definition $(72)_2$ and $(74)_2$, we have

$$\frac{\partial \bar{\tau}_{\mathrm{tr}}}{\partial \bar{\mathbf{E}}^{\mathrm{e}}_{\mathrm{tr}}} = \frac{1}{\sqrt{2}} \left(\frac{\partial \mathbf{T}^{\mathrm{K}}_{0,\mathrm{tr}}}{\partial \bar{\mathbf{E}}^{\mathrm{e}}_{\mathrm{tr}}} \right)^{\top} \left(\frac{\partial \left|\mathbf{T}^{\mathrm{K}}_{0,\mathrm{tr}}\right|}{\partial \mathbf{T}^{\mathrm{K}}_{0,\mathrm{tr}}} \right) = \sqrt{2} S \left(\mathbb{I} - \frac{1}{3} \mathbf{1} \otimes \mathbf{1} \right) \underbrace{\frac{\mathbf{T}^{\mathrm{K}}_{0,\mathrm{tr}}}{\left|\mathbf{T}^{\mathrm{K}}_{0,\mathrm{tr}}\right|}}_{=\bar{\mathbf{N}}^{\mathrm{p}}_{\mathrm{tr}}} = \sqrt{2} S \bar{\mathbf{N}}^{\mathrm{p}}_{\mathrm{tr}}. \tag{75}$$

Similarly, using the definition $(71)_2$, we have

$$\frac{\partial \bar{\mathbf{N}}^{\mathrm{p}}_{\mathrm{tr}}}{\partial \bar{\mathbf{E}}^{\mathrm{e}}_{\mathrm{tr}}} = \frac{\sqrt{2} S}{\bar{\tau}_{\mathrm{tr}}} \left[\left(\mathbb{I} - \frac{1}{3} \mathbf{1} \otimes \mathbf{1} \right) - \bar{\mathbf{N}}^{\mathrm{p}}_{\mathrm{tr}} \otimes \bar{\mathbf{N}}^{\mathrm{p}}_{\mathrm{tr}} \right]. \tag{76}$$

Turning to the calculation of the derivative $(\partial \bar{\tau}_{\mathrm{n}+1} / \partial \bar{\mathbf{E}}^{\mathrm{e}}_{\mathrm{tr}})$, we note that $\bar{\mathbf{E}}^{\mathrm{e}}_{\mathrm{tr}}$ enters the equations through $\bar{\tau}_{\mathrm{tr}}$ and $\bar{p}_{\mathrm{tr}}$, so that, using (75), we have

$$\frac{\partial \bar{\tau}_{\mathrm{n}+1}}{\partial \bar{\mathbf{E}}^{\mathrm{e}}_{\mathrm{tr}}} = \frac{\partial \bar{\tau}_{\mathrm{n}+1}}{\partial \bar{\tau}_{\mathrm{tr}}} \frac{\partial \bar{\tau}_{\mathrm{tr}}}{\partial \bar{\mathbf{E}}^{\mathrm{e}}_{\mathrm{tr}}} + \frac{\partial \bar{\tau}_{\mathrm{n}+1}}{\partial \bar{p}_{\mathrm{tr}}} \frac{\partial \bar{p}_{\mathrm{tr}}}{\partial \bar{\mathbf{E}}^{\mathrm{e}}_{\mathrm{tr}}} = \sqrt{2} S \frac{\partial \bar{\tau}_{\mathrm{n}+1}}{\partial \bar{\tau}_{\mathrm{tr}}} \bar{\mathbf{N}}^{\mathrm{p}}_{\mathrm{tr}} - B \frac{\partial \bar{\tau}_{\mathrm{n}+1}}{\partial \bar{p}_{\mathrm{tr}}} \mathbf{1}. \tag{77}$$

Copyright © 0000 John Wiley & Sons, Ltd.

Prepared using nmeauth.cls
DOI: 10.1002/nme

Finally, using (74), (75), (76), and (77) in (73) and rearranging, we have

$$\boldsymbol{\mathcal{D}} = 2S\left(\frac{\bar{\tau}_{\mathrm{n+1}}}{\bar{\tau}_{\mathrm{tr}}}\right)\left(\mathbb{I} - \frac{1}{3}\mathbf{1}\otimes\mathbf{1}\right) + B\mathbf{1}\otimes\mathbf{1} - 2S\left(\frac{\bar{\tau}_{\mathrm{n+1}}}{\bar{\tau}_{\mathrm{tr}}} - \frac{\partial\bar{\tau}_{\mathrm{n+1}}}{\partial\bar{\tau}_{\mathrm{tr}}}\right)\bar{\mathbf{N}}^{\mathrm{p}}_{\mathrm{tr}}\otimes\bar{\mathbf{N}}^{\mathrm{p}}_{\mathrm{tr}} - \sqrt{2}B\frac{\partial\bar{\tau}_{\mathrm{n+1}}}{\partial\bar{p}_{\mathrm{tr}}}\bar{\mathbf{N}}^{\mathrm{p}}_{\mathrm{tr}}\otimes\mathbf{1}, \quad (78)$$

where $(\partial\bar{\tau}_{\mathrm{n+1}}/\partial\bar{\tau}_{\mathrm{tr}})$ and $(\partial\bar{\tau}_{\mathrm{n+1}}/\partial\bar{p}_{\mathrm{tr}})$ are calculated straightforwardly from (56) as

$$\frac{\partial\bar{\tau}_{\mathrm{n+1}}}{\partial\bar{\tau}_{\mathrm{tr}}} = \frac{\bar{p}_{\mathrm{tr}}}{\bar{p}_{\mathrm{tr}} + S\Delta t g_{\mathrm{n+1}}} \quad \text{and} \quad \frac{\partial\bar{\tau}_{\mathrm{n+1}}}{\partial\bar{p}_{\mathrm{tr}}} = \frac{\bar{\tau}_{\mathrm{tr}}S\Delta t g_{\mathrm{n+1}}}{(\bar{p}_{\mathrm{tr}} + S\Delta t g_{\mathrm{n+1}})^2}, \quad (79)$$

respectively.

The tangents $\mathbf{K}^{AB}_{\mathbf{u}g}$: In component form, the tangents $K^{AB}_{u_i g}$ are given by

$$K^{AB}_{u_i g} = \int_{\mathcal{B}^{\mathrm{e}}}\left(\frac{\partial N^A}{\partial x_j}\Lambda_{ij}N^B\right)dv, \quad (80)$$

where

$$\boldsymbol{\Lambda} = \frac{\partial\mathbf{T}_{\mathrm{n+1}}}{\partial g_{\mathrm{n+1}}}. \quad (81)$$

Considering (70) and the relation $\mathbf{T}_{\mathrm{n+1}} = J^{-1}_{\mathrm{n+1}}\mathbf{T}^{\mathrm{K}}_{\mathrm{n+1}}$ and recalling that $\mathbf{T}^{\mathrm{K}}_{\mathrm{tr}}$, $\bar{\tau}_{\mathrm{tr}}$, and $\bar{\mathbf{N}}^{\mathrm{p}}_{\mathrm{tr}}$ only depend on the displacement degrees of freedom, we have that

$$\boldsymbol{\Lambda} = \frac{\sqrt{2}}{J_{\mathrm{n+1}}}\frac{\partial\bar{\tau}_{\mathrm{n+1}}}{\partial g_{\mathrm{n+1}}}\bar{\mathbf{N}}^{\mathrm{p}}_{\mathrm{tr}}, \quad (82)$$

where from (56),

$$\frac{\partial\bar{\tau}_{\mathrm{n+1}}}{\partial g_{\mathrm{n+1}}} = \frac{-\bar{\tau}_{\mathrm{tr}}\bar{p}_{\mathrm{tr}}S\Delta t}{(\bar{p}_{\mathrm{tr}} + S\Delta t g_{\mathrm{n+1}})^2}. \quad (83)$$

The tangents $\mathbf{K}^{AB}_{g\mathbf{u}}$: The tangents $K^{AB}_{gu_k}$ are

$$K^{AB}_{gu_k} = -\int_{\mathcal{B}^{\mathrm{e}}}\left[-\frac{\partial N^A}{\partial x_j}\left(\delta_{jl}\frac{\partial g}{\partial x_k} + \delta_{jk}\frac{\partial g}{\partial x_l} - \delta_{kl}\frac{\partial g}{\partial x_j}\right)\frac{\partial N^B}{\partial x_l} + N^A\Gamma_{kl}\frac{\partial N^B}{\partial x_l}\right]dv, \quad (84)$$

where

$$\Gamma_{kl} = F_{lq}\frac{\partial g_{\mathrm{res}}}{\partial F_{kq}} + g_{\mathrm{res}}\delta_{kl} \quad \text{and} \quad g_{\mathrm{res}} = \frac{g_{\mathrm{n+1}} - g^{\mathrm{loc}}_{\mathrm{n+1}}}{\xi^2_{\mathrm{n+1}}}. \quad (85)$$

Application of the chain rule yields the following expression for Γ_{kl}:

$$\Gamma_{kl} = \frac{1}{2}\frac{\partial g_{\mathrm{res}}}{\partial\bar{E}^{\mathrm{e}}_{\mathrm{tr},mn}}\mathcal{L}_{mnpq}\mathcal{B}_{pqkl} + g_{\mathrm{res}}\delta_{kl} \quad (86)$$

with $\boldsymbol{\mathcal{L}}$ and $\boldsymbol{\mathcal{B}}$ defined in (69). With g_{res} given through $(85)_2$ and (65), we may write $g_{\mathrm{res}} = g_{\mathrm{res}}(\bar{\tau}_{\mathrm{n+1}}, \bar{p}_{\mathrm{tr}})$, so that

$$\frac{\partial g_{\mathrm{res}}}{\partial\bar{\mathbf{E}}^{\mathrm{e}}_{\mathrm{tr}}} = \frac{\partial g_{\mathrm{res}}}{\partial\bar{\tau}_{\mathrm{n+1}}}\frac{\partial\bar{\tau}_{\mathrm{n+1}}}{\partial\bar{\mathbf{E}}^{\mathrm{e}}_{\mathrm{n+1}}} - B\frac{\partial g_{\mathrm{res}}}{\partial\bar{p}_{\mathrm{tr}}}\mathbf{1}, \quad (87)$$

which may be used with (77) to complete the calculation.

Copyright © 0000 John Wiley & Sons, Ltd.
Prepared using nmeauth.cls

DOI: 10.1002/nme

The tangents $\mathbf{K}_{gg}^{AB}$: Finally, the tangents K_{gg}^{AB} are

$$K_{gg}^{AB} = -\int_{\mathrm{B}} \left[\frac{\partial N^A}{\partial x_j} \frac{\partial N^B}{\partial x_j} + N^A \frac{\partial g_{\mathrm{res}}}{\partial g_{\mathrm{n+1}}} N^B \right] dv_{\mathrm{R}}, \tag{88}$$

with

$$\frac{\partial g_{\mathrm{res}}}{\partial g_{\mathrm{n+1}}} = \frac{\partial g_{\mathrm{res}}}{\partial \bar{\tau}_{\mathrm{n+1}}} \frac{\partial \bar{\tau}_{\mathrm{n+1}}}{\partial g_{\mathrm{n+1}}} \tag{89}$$

and $(\partial \bar{\tau}_{\mathrm{n+1}}/\partial g_{\mathrm{n+1}})$ given through (83).

6. VERIFICATION AND CONVERGENCE

In this section, we verify our finite-element (FE) implementation and demonstrate convergence and the absence of mesh-sensitivity. We first consider two settings with simple quasi-one-dimensional solutions that allow for verification of our elements by comparing with finite-difference (FD) solutions. These configurations are (i) linear shear flow with gravity and (ii) annular shear flow without gravity. We also show that our FE solutions converge faster than linearly with the mesh resolution and that our consistent tangents yield asymptotically quadratic convergence of the Newton procedure. Finally, to fully demonstrate all salient features of the model in a more complex setting, we consider the case of annular shear flow with gravity using both element types and show that the calculation results using the nonlocal model are mesh-insensitive in contrast to simulations using the local inertial rheology. In all cases, we refer to spatial regions where flow localizes as shear bands. To be clear, these are not shear bands induced by material instabilities [37, 23, 36, 54, 55] but shear bands arising due to inhomogeneous stress fields.

Material parameters: Throughout, we use material parameters corresponding to glass beads. Based on the work of [56], we take the local parameters to be

$$\mu_{\mathrm{s}} = 0.3819 \quad \text{and} \quad b = 0.9377,$$

and based on our previous work [14], we take the nonlocal amplitude to be

$$A = 0.48.$$

Further, we take $\rho_{\mathrm{s}} = 2450\,\mathrm{kg/m^3}$ and $d = 1\,\mathrm{mm}$; however, all results in subsequent sections will be presented in dimensionless form, and hence, the numerical values of ρ_{s} and d are inconsequential. Finally, for the elastic parameters, we take $S = 1\,\mathrm{MPa}$ and $B = 10\,\mathrm{MPa}$. As mentioned previously, these parameters have absolutely no effect on the simulated steady flow fields. They essentially function as numerical parameters that may be tuned to attain good numerical performance. If the elastic moduli are too low, one must subject the simulated granular media to a large amount of strain in order to complete the process of yielding and reach steady-state. However, if they are too high, numerical convergence is slowed. We have found that the aforementioned numerical values provide a reasonable compromise between these two issues.

Fluidity boundary conditions: The nonlocal granular rheology requires that the non-standard fluidity boundary conditions (25) be specified. This issue arises in virtually all nonlocal constitutive approaches [17, 18, 21, 20, 49, 50, 22], and motivating these non-standard boundary conditions from a physical perspective can be challenging. A rough physical intuition may be ascribed to the fluidity boundary conditions for the case of a wall boundary. For example, the wall at the boundary of a granular body may be specified in a number of ways, such as through a smooth but frictional wall, a wall of a certain roughness, or a layer of grains of a certain size glued to a wall. This wall condition can then affect flow near the wall, such as in slippage between grains and the wall. In our previous work [14], we considered flow configurations with walls made up of a layer of glued

Copyright © 0000 John Wiley & Sons, Ltd.
Prepared using nmeauth.cls

DOI: 10.1002/nme

grains – a condition which yields no slippage and minimal wall effects in general. For this situation, we have found that homogeneous Neumann boundary conditions for the fluidity ($\hat{\zeta} = 0$) provide an excellent description of experiments. Regarding free surface boundaries, we feel confident that the same homogeneous Neumann condition is appropriate, due to the similarity of a free surface to a symmetry plane. For these reasons, we will predominantly use this fluidity boundary condition for the calculations reported in this section. It bears noting, however, that in some cases – particularly for thin granular layers – a homogeneous Dirichlet fluidity boundary condition ($g = 0$) may be more appropriate. For example, in our previous work [57], we have shown that in gravity-driven flow down a rough inclined plane a homogeneous Dirichlet condition yields fluidity fields that are lower than those obtained when homogeneous Neumann boundary conditions are utilized, which can quantitatively account for the size-dependent strengthening seen in experiments [58, 59, 1]. Consistent with the focus of the present work, we will demonstrate that our implementation is capable of handling all types of fluidity boundary conditions by showing mesh convergence for both $\hat{\zeta} = 0$ and $g = 0$ fluidity boundary conditions. A more concrete understanding of the physics of the fluidity boundary condition will require detailed experiments and discrete-element method calculations to probe the relationship between the wall condition and the fluidity, and recent work has begun to address this open research question [60, 61].

6.1. Linear shear flow with gravity

We use the case of linear shear flow with gravity to verify our linear three-dimensional (3D) element. In this configuration, a rough plate is dragged horizontally across a deep bed (infinite half-space) of gravitationally-loaded granular material, shown schematically in Fig. 1(a). The weight of the plate imposes a pressure P_{wall} on the $z = 0$ surface, and its motion imposes a horizontal velocity of v_{wall}. Due to the gravitational pressure gradient in the z-direction, the minimum pressure in the granular bed occurs just beneath the plate, and hence, we expect a shear band to develop there, decaying into the bulk of the granular bed. Through dimensional analysis, we identify two important dimensionless groups which will quantitatively set the flow field: (i) the dimensionless wall pressure, $P_{\text{wall}}/\phi\rho_{\text{s}}Gd$, and (ii) the dimensionless wall velocity, $v_{\text{wall}}/\sqrt{Gd}$. Finally, since we cannot truly simulate an infinite granular bed, we must specify a finite depth. We consider a granular bed that is sufficiently deep so that the flow field is depth-independent. We find that a depth of $20d$ yields depth-independent results for the values of $P_{\text{wall}}/\phi\rho_{\text{s}}Gd$ and $v_{\text{wall}}/\sqrt{Gd}$ considered here and use this throughout.

First, in order to verify the 3D element, we utilize a FD-based solution for comparison. The stress field in this configuration is quite simple – statically-determinant, in fact, when one considers a shear stress boundary condition τ_{wall} rather than the kinematic velocity boundary condition. Then, the equivalent shear stress is spatially-constant and given by the shear stress imparted by the wall, $\bar{\tau} = \tau_{\text{wall}}$, and the pressure field is a combination of the wall pressure, P_{wall}, and the gravitational pressure gradient, so that $\bar{p} = P_{\text{wall}} + \phi\rho_{\text{s}}Gz$. Since the fields only vary in z, (23) reduces to

$$\frac{\partial^2 g}{\partial z^2} = \frac{1}{\xi^2(\mu)}\left(g - g_{\text{loc}}(\bar{p},\mu)\right) \quad \text{with} \quad \bar{p} = P_{\text{wall}} + \phi\rho_{\text{s}}Gz \quad \text{and} \quad \mu = \frac{\mu_{\text{wall}}}{1 + \phi\rho_{\text{s}}Gz/P_{\text{wall}}}, \tag{90}$$

where $\mu_{\text{wall}} = \tau_{\text{wall}}/P_{\text{wall}}$ is the stress ratio at the wall. With homogeneous Neumann boundary conditions for g taken at $z = 0$ and a depth of $z = 20d$, the g-field may be easily obtained through finite-differences. Multiplying the g-field with the known μ-field gives the $\dot{\gamma}^{\text{p}}$-field. We assume that at steady state elastic strains are fixed, so that

$$\dot{\gamma}^{\text{p}} \approx \dot{\gamma} = \frac{dv}{dz}.$$

Integrating and enforcing $v = 0$ at the bottom of the bed ($z = 20d$) gives the FD steady-state velocity field. Since the FD solution is obtained in "force control," the wall stress ratio μ_{wall} may be iteratively adjusted to obtain the desired v_{wall}. In our FD calculations, a very fine step size of $0.01d$ is used.

Copyright © 0000 John Wiley & Sons, Ltd.
Prepared using nmeauth.cls

DOI: 10.1002/nme

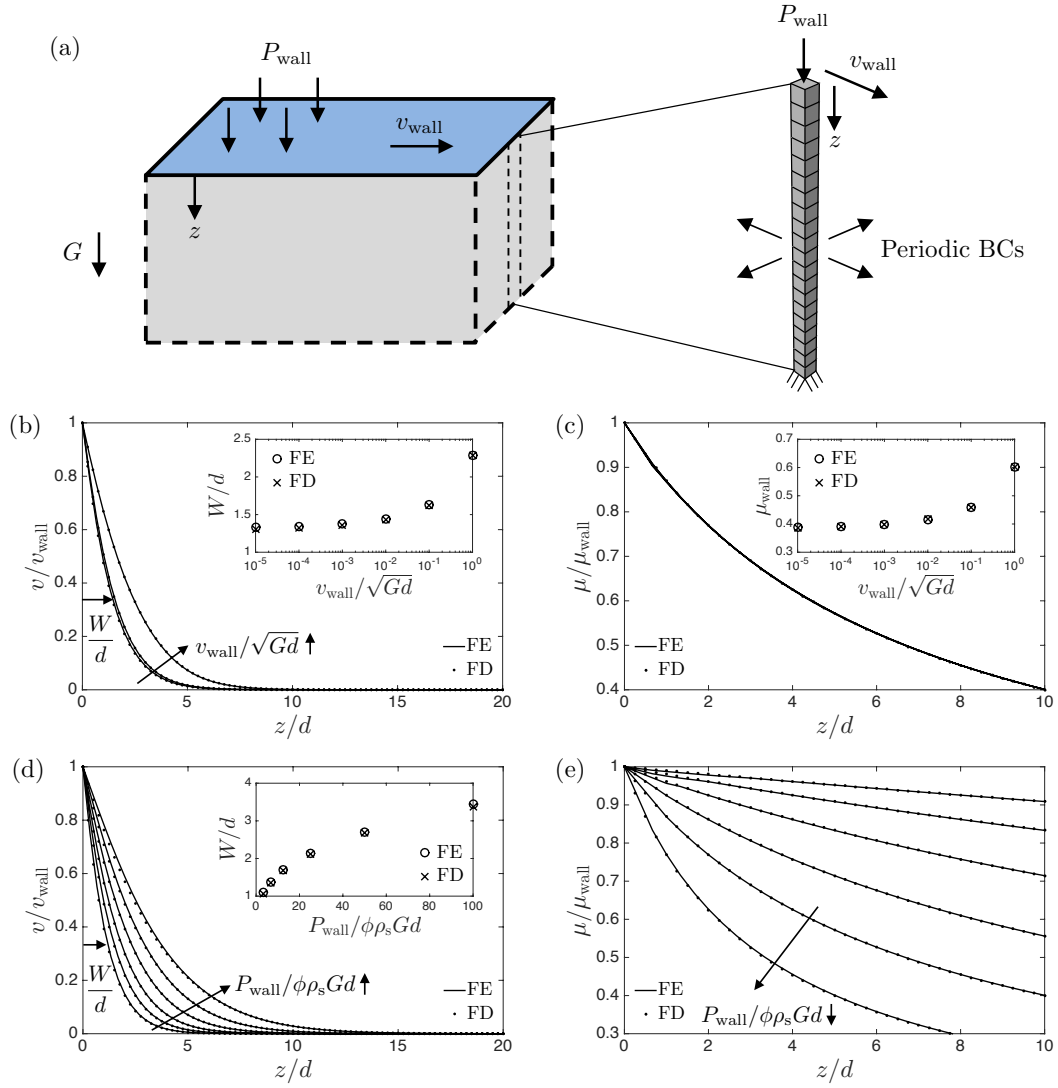

Figure 1. Simulation results for linear shear flow with gravity. (a) Schematic and finite-element mesh. (b) Flow fields obtained from finite-element (FE) and finite-difference (FD) calculations for $P_{\rm wall}/\phi\rho_{\rm s}Gd = 6.67$ and $v_{\rm wall}/\sqrt{Gd} = 10^{-4}, 10^{-2}$, and 1. Inset: Normalized shear band width W/d as a function of $v_{\rm wall}/\sqrt{Gd}$. (c) μ-fields for $P_{\rm wall}/\phi\rho_{\rm s}Gd = 6.67$ and all values of $v_{\rm wall}/\sqrt{Gd}$. Inset: $\mu_{\rm wall}$ as a function of $v_{\rm wall}/\sqrt{Gd}$. (d) Flow fields in the rate-independent regime ($v_{\rm wall}/\sqrt{Gd} = 10^{-3}$) for $P_{\rm wall}/\phi\rho_{\rm s}Gd = 3.33, 6.67, 12.5, 25, 50$, and 100. Inset: Normalized shear band width as a function of $\phi\rho_{\rm s}Gd/P_{\rm wall}$. (e) μ-fields for $v_{\rm wall}/\sqrt{Gd} = 10^{-3}$ and $P_{\rm wall}/\phi\rho_{\rm s}Gd = 3.33, 6.67, 12.5, 25, 50$, and 100.

For the FE calculations, we consider a mesh consisting of a single column of 3D finite elements in the z-direction, shown in Fig. 1(a) for the case of a mesh of 20 elements and a mesh resolution of $h/d = 1$, where h is the mesh size in the z-direction. On the bottom of the bed ($z = 20d$), all displacement degrees of freedom are set to be zero, while on the top, the lateral degrees of freedom are specified to impose the lateral wall velocity $v_{\rm wall}$, while leaving u_z unconstrained. A normal traction at $z = 0$ imposes the wall pressure $P_{\rm wall}$. Homogeneous Neumann fluidity boundary conditions ($\hat{\zeta} = 0$) are taken at both the top and bottom, and periodic boundary conditions for all fields are enforced in the lateral directions. The velocity field is determined through the increments in the displacement field and the wall stress ratio $\mu_{\rm wall}$ through the reaction forces at the nodes where the wall velocity $v_{\rm wall}$ is prescribed. Calculations are run until the velocity field and $\mu_{\rm wall}$ no longer

Copyright © 0000 John Wiley & Sons, Ltd.
Prepared using nmeauth.cls

DOI: 10.1002/nme

change in time, indicating that steady-state has been attained. We find that a wall displacement of d is sufficient to ensure that these conditions are met. In the subsequent calculations, we fix the mesh size at $h/d = 1/3$. We will revisit the effect of mesh size at the end of this section.

First, we fix $P_{\text{wall}}/\phi\rho_{\text{s}}Gd = 6.67$ and examine the effect of the wall speed, $v_{\text{wall}}/\sqrt{Gd}$. The calculated flow fields are summarized in Fig. 1(b). The velocity field as a function of z for $v_{\text{wall}}/\sqrt{Gd} = 10^{-4}, 10^{-2}$ and 1 are shown in the main plot. The solid line denotes the FE solution and the dashed line denotes the FD solution, which match well. The velocity fields display a decaying, exponential character (although they are not precisely exponential functions) with flow concentrated immediately beneath the plate in a shear band as expected. To characterize the size of the flowing zone, we define the shear band width W as the value of depth z at which the velocity has decayed to $e^{-1} = 0.368$ of the wall value. The normalized shear band width W/d is plotted as a function of $v_{\text{wall}}/\sqrt{Gd}$ from 10^{-5} to 1 in the inset of Fig. 1(b). We note that for sufficiently small values of wall speed ($v_{\text{wall}}/\sqrt{Gd} \lesssim 10^{-3}$) the shear band width approaches a rate-independent plateau value, while for higher wall speeds ($v_{\text{wall}}/\sqrt{Gd} \gtrsim 10^{-2}$) the shear band width is strongly rate-dependent. This rate-independent to rate-dependent transition as the driving rate is increased is indicative of the transition from the quasi-static to inertial regimes of flow. Mathematically, in the rate-independent regime, the nonlocal term, $\nabla^2 g$, dominates the the local term, g_{loc}, in (23) in almost all of the spatial domain. The remaining nonlocal relation, $\nabla^2 g = g/\xi^2$, is rate-independent in that the g-field may be scaled by an arbitrary constant to accommodate changes in the velocity boundary condition without changes in the stress field. However, in the rate-dependent regime, the local term dominates, $g \approx g_{\text{loc}}$, so that the model approaches the prediction of the local inertial rheology. It bears noting that the purely local model would predict that $W/d \to 0$ as $v_{\text{wall}}/\sqrt{Gd} \to 0$, contrary to experimental observations [62]. Likewise, a rate-independent plasticity model, like Drucker-Prager, would predict a shear band width of 0, and hence, calculations based on such a model would produce highly mesh-dependent solutions. The nonlocal model remedies this issue. What is more, the model is quantitatively predictive (see Fig. 4(b) of [14] for $P_{\text{wall}}/\phi\rho_{\text{s}}Gd = 6.86$ and $v_{\text{wall}}/\sqrt{Gd} = 3 \times 10^{-3}$). The normalized FE μ-fields are shown in Fig. 1(c) along with the analytical μ-field used in the FD solution $(90)_3$, which is independent of the wall speed, only depending on $P_{\text{wall}}/\phi\rho_{\text{s}}Gd$, and the fields match well. The wall stress ratio μ_{wall} as a function of $v_{\text{wall}}/\sqrt{Gd}$ from 10^{-5} to 1 is shown in the inset of Fig. 1(c). Recall that in the FE calculations v_{wall} is prescribed, and μ_{wall} is determined from nodal reaction forces, while in the FD calculations μ_{wall} is prescribed, and v_{wall} is determined from the calculated flow fields. Despite the fact that the FE calculations are in "kinematic control," while the FD calculations are in "force control," the same relationship between μ_{wall} and $v_{\text{wall}}/\sqrt{Gd}$ is obtained. Similar to the situation for the shear band width W/d, the wall stress ratio approaches a rate-independent plateau of μ_{s} for sufficiently small wall speeds, while it is rate-dependent and increasing for higher wall speeds.

Next, we examine the effect of wall pressure in the rate-independent regime, fixing $v_{\text{wall}}/\sqrt{Gd} = 10^{-3}$, and taking $P_{\text{wall}}/\phi\rho_{\text{s}}Gd = 3.33, 6.67, 12.5, 25, 50,$ and 100. In this flow configuration, the parameter $P_{\text{wall}}/\phi\rho_{\text{s}}G$ may be thought of as a length-dimensioned system "size," and hence any dependence of the flow field on $P_{\text{wall}}/\phi\rho_{\text{s}}Gd$ is evidence of finite-size effects. Both FE and FD flow field solutions are shown in Fig. 1(d), verifying the 3D FE implementation, and the normalized shear band width W/d is plotted as a function of $P_{\text{wall}}/\phi\rho_{\text{s}}Gd$ in the inset. In the limit that the wall pressure (and hence the pressure at $z = 0$) goes to zero, the pressure gradient dominates the characteristic pressure at the wall, and the shear band width also goes to zero. As the wall pressure is increased relative to the gravitational pressure, the characteristic pressure at the wall becomes comparable to the pressure gradient, and the shear band width increases. In the limit of $P_{\text{wall}}/\phi\rho_{\text{s}}Gd \to \infty$, the shear band would grow to reach the bottom of the granular bed, and a state of homogeneous simple shear with approximately spatially constant pressure given by P_{wall} would be achieved. Here, we only consider wall pressures that are small enough so that all flow fields are unaffected by the bottom of the granular bed. The normalized FE μ-fields are shown in Fig. 1(e), which compare favorably to the corresponding μ-fields used in FD solutions $(90)_3$ and clearly show the dependence of the μ-field on $P_{\text{wall}}/\phi\rho_{\text{s}}Gd$. Since we have focused on the rate-independent regime here, the wall stress ratio μ_{wall} remains close to μ_{s} for all values of $P_{\text{wall}}/\phi\rho_{\text{s}}Gd$ considered.

Copyright © 0000 John Wiley & Sons, Ltd.
Prepared using nmeauth.cls

DOI: 10.1002/nme

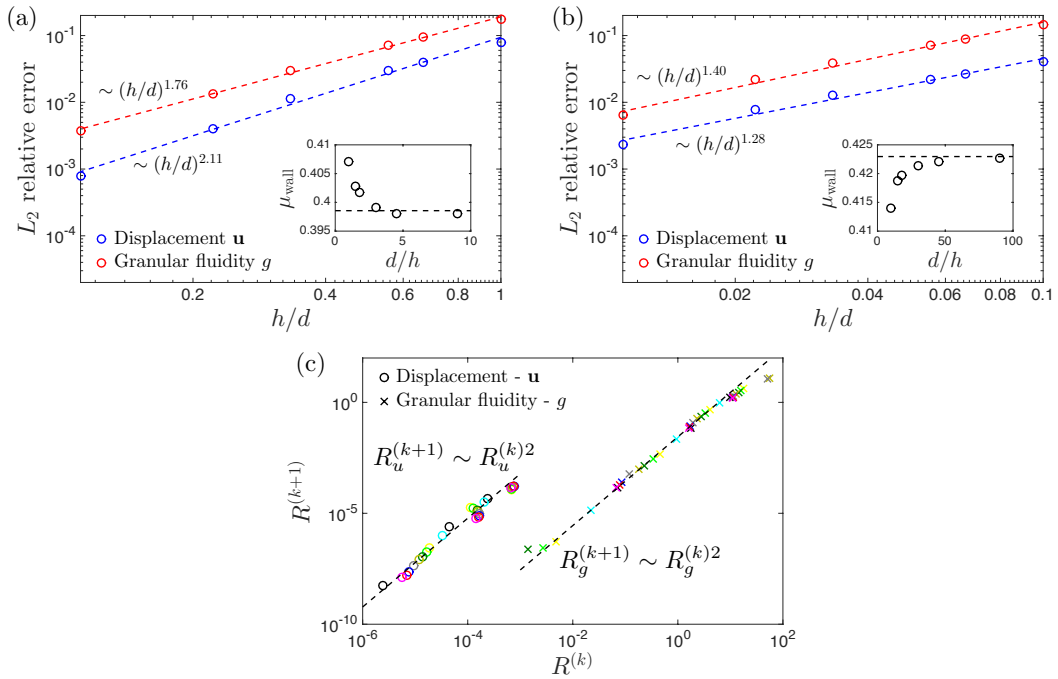

Figure 2. (a) Demonstration of mesh convergence for linear shear flow with gravity for $P_{\rm wall}/\phi\rho_{\rm s}Gd = 6.67$ and $v_{\rm wall}/\sqrt{Gd} = 10^{-3}$. L_2-norm of the relative error as a function of the normalized mesh resolution h/d for the displacement and granular fluidity fields. Inset: Normalized wall reaction force $\mu_{\rm wall}$ as a function of mesh resolution. The "exact" solution is denoted by the horizontal dashed line. (b) Convergence test repeated for the case of a homogeneous Dirichlet ($g = 0$) wall fluidity boundary condition. (c) Demonstration of asymptotically quadratic convergence of the Newton procedure. The colors of the markers denote unique increments, and the dashed lines denote a quadratic power law.

Finally, we consider the numerical performance of our 3D implementation, demonstrating mesh convergence of our simulation results and asymptotically quadratic convergence of the Newton procedure for the specific case of $P_{\rm wall}/\phi\rho_{\rm s}Gd = 6.67$ and $v_{\rm wall}/\sqrt{Gd} = 10^{-3}$. For a mesh convergence study, one would typically compare FE solutions obtained using different mesh resolutions to an exact solution. Since we have no exact solution, we use the FE solution obtained using a very fine mesh of $h_{\rm exact}/d = 1/90$ as our reference, "exact" solution. We then consider mesh resolutions of $h/d = 1/9, 2/9, 1/3, 5/9, 2/3$, and 1 and run each simulation to steady-state. Each solution is compared to the "exact" solution, using a definition of the relative error based on the discrete L_2-norm, defined for the displacement field as

$$\frac{||\mathbf{u}_{\rm FE} - \mathbf{u}_{\rm exact}||_2}{||\mathbf{u}_{\rm exact}||_2} = \frac{\sqrt{\sum_{A=1}^{n} T_A |\mathbf{u}_{\rm FE}^A - \mathbf{u}_{\rm exact}^A|^2 h}}{\sqrt{\sum_{A=1}^{n_{\rm exact}} T_A |\mathbf{u}_{\rm exact}^A|^2 h_{\rm exact}}}, \tag{91}$$

where $T_A = 1/2$ at the endpoints of the domain and $T_A = 1$ otherwise, so that the sum calculates the trapezoid rule. An analogous definition is used for the granular fluidity field. The L_2-norm of the relative error as a function of the mesh resolution, h/d, is shown in Fig. 2(a) for the displacement field $\mathbf{u}$ and the granular fluidity field g. Both fields converge at at least a linear rate, as expected for the linear finite elements used here. The wall stress ratio $\mu_{\rm wall}$ determined through nodal reaction forces is also plotted as a function of d/h in the inset of Fig. 2(a), showing that the reaction forces also converge to the "exact" solution, denoted by the horizontal dashed line. Thus far, we have only considered boundary-value problems involving homogeneous Neumann boundary conditions for the granular fluidity. To show that our FE implementation can handle situations involving mixed fluidity boundary conditions, we consider the case in which a homogeneous Dirichlet ($g = 0$) boundary

Copyright © 0000 John Wiley & Sons, Ltd.
Prepared using nmeauth.cls

DOI: 10.1002/nme

condition is specified at the wall ($z = 0$) and $P_{\text{wall}}/\phi\rho_{\text{s}}Gd = 6.67$ and $v_{\text{wall}}/\sqrt{Gd} = 10^{-3}$ as before. We then repeat our mesh convergence test for this case and summarize the results in Fig. 2(b). The $g = 0$ boundary condition induces a boundary layer at the wall, in which the fluidity field varies rapidly in space, necessitating the finer range of mesh resolutions considered in Fig. 2(b). (The "exact" solution for this case is obtained using a mesh resolution of $h_{\text{exact}}/d = 1/900$.) Again, we see that both the displacement field $\mathbf{u}$ and the granular fluidity field g converge at at least a linear rate and that the wall stress ratio converges to the "exact" solution. While imposing a $g = 0$ boundary condition at the wall may not yield a realistic flow in this configuration, it is useful to confirm that our FE implementation continues to be valid. In a final consideration of numerical performance, we return to the homogeneous Neumann boundary condition case and demonstrate asymptotically quadratic convergence of the Newton procedure by considering the L_∞-norms of the global (assembled) displacement and fluidity residuals. Each norm is normalized by the average element-level nodal contribution to the respective global residuals, and the normalized displacement and fluidity residual norms for the kth Newton procedure iterate of a given increment are denoted as $R_u^{(k)}$ and $R_g^{(k)}$, respectively. To demonstrate asymptotically quadratic convergence, it is sufficient to show that $R^{(k+1)} \sim R^{(k)2}$ for displacement and fluidity within an increment as the residuals approach zero.** We choose ten increments, which occur during the process of yielding prior to reaching steady-state, i.e., the most demanding situation for the numerical procedure, and plot $R^{(k+1)}$ versus $R^{(k)}$ for both displacement and granular fluidity in Fig. 2(c). Each unique increment is denoted with a different color, and quadratic power-laws are plotted with dashed lines. Asymptotically quadratic convergence is evident for both the displacement and fluidity residuals, verifying the algorithmically consistent tangents.

6.2. *Annular shear flow without gravity*

Next, we use the case of annular shear flow without gravity to verify our generalized axisymmetric (GAX) element. In this configuration, shown schematically in 3(a), an annular shear cell with rough inner and outer walls of radii R_{i} and R_{o}, respectively, is filled with grains. A pressure P_{wall} is applied to the outer wall, and the outer wall is constrained from rotating ($\theta = 0$), while the inner wall is prevented from moving radially ($u_r = 0$). A rotation rate Ω is then applied to the inner wall. In this configuration, the shear stress will decay with radial position, and hence, we expect a shear band to develop at the inner wall, decaying radially. Again dimensional analysis allows us to identify two important dimensionless groups: (i) the dimensionless inner wall radius, R_{i}/d, and (ii) the dimensionless inner wall velocity, $R_{\text{i}}\Omega\sqrt{\rho_{\text{s}}/P_{\text{wall}}}$. In all calculations, we choose an outer wall radius that is sufficiently large so that the flow field is independent of this parameter. We find that $(R_{\text{o}} - R_{\text{i}}) = 20d$ satisfies this condition in all cases considered here.

As in the previous section, in order the verify the GAX element, we need a FD-based solution for comparison. In this configuration, the pressure is constant and given by P_{wall}. While this may not be obvious from the outset, it has been routinely seen in discrete element method (DEM) calculations [7, 13]. Balancing moments gives a decaying shear stress field of $\bar{\tau} = \tau_{\text{wall}}(R_{\text{i}}/r)^2$, where τ_{wall} is the shear stress applied to the inner wall. All fields only vary in r, so that (23) reduces to

$$\frac{\partial^2 g}{\partial r^2} + \frac{1}{r}\frac{\partial g}{\partial r} = \frac{1}{\xi^2(\mu)}\left(g - g_{\text{loc}}(\bar{p}, \mu)\right) \quad \text{with} \quad \bar{p} = P_{\text{wall}} \quad \text{and} \quad \mu = \mu_{\text{wall}}\left(\frac{R_{\text{i}}}{r}\right)^2, \tag{92}$$

where $\mu_{\text{wall}} = \tau_{\text{wall}}/P_{\text{wall}}$ is the wall stress ratio. Homogeneous Neumann boundary conditions for g are taken at $r = R_{\text{i}}$ and R_{o}, and the g-field is calculated through finite differences. The shear strain rate, $\dot{\gamma}^{\text{p}} \approx \dot{\gamma} = dv/dr$, is given through multiplying the calculated g-field with the known μ-field. Integrating and enforcing $v = 0$ at the outer wall gives the FD steady-state velocity field. The wall stress ratio μ_{wall} is adjusted to obtain the desired v_{wall} for comparison to FE results. Again, a very fine step size of $0.01d$ is used.

**Typically, the rate of convergence is assessed through the error in the degrees of freedom, but since the residuals are asymptotically linear in the degree of freedom error near the root, and residual values for each iterate are more readily available in Abaqus, we use the residual as a surrogate.

Copyright © 0000 John Wiley & Sons, Ltd.
Prepared using nmeauth.cls

DOI: 10.1002/nme

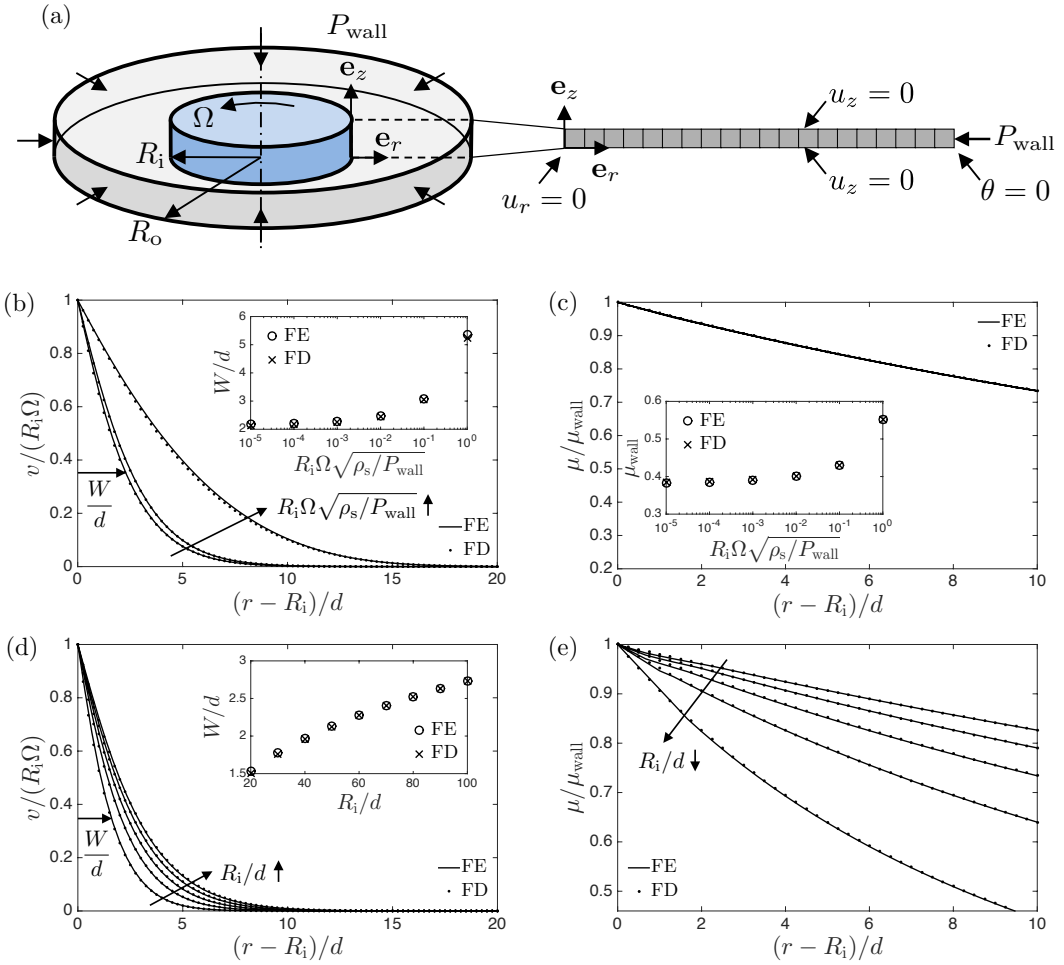

Figure 3. Simulation results for annular shear flow without gravity. (a) Schematic and finite-element mesh. (b) Flow fields obtained from finite-element (FE) and finite-difference (FD) calculations for $R_{\rm i}/d = 60$ and $R_{\rm i}\Omega\sqrt{\rho_{\rm s}/P_{\rm wall}} = 10^{-4}, 10^{-2}$, and 1. Inset: Normalized shear band width W/d as a function of $R_{\rm i}\Omega\sqrt{\rho_{\rm s}/P_{\rm wall}}$. (c) μ-fields for $R_{\rm i}/d = 60$ and all values of $R_{\rm i}\Omega\sqrt{\rho_{\rm s}/P_{\rm wall}}$. Inset: $\mu_{\rm wall}$ as a function of $R_{\rm i}\Omega\sqrt{\rho_{\rm s}/P_{\rm wall}}$. (d) Flow fields in the rate-independent regime ($R_{\rm i}\Omega\sqrt{\rho_{\rm s}/P_{\rm wall}} = 10^{-3}$) for $R_{\rm i}/d = 20, 40, 60, 80,$ and 100. Inset: Normalized shear band width as a function of $R_{\rm i}/d$. (e) μ-fields for $R_{\rm i}\Omega\sqrt{\rho_{\rm s}/P_{\rm wall}} = 10^{-3}$ and $R_{\rm i}/d = 20, 40, 60, 80,$ and 100.

We consider a FE mesh which consists of a single row of GAX elements in the r-direction, shown in 3(a) for the case of a mesh of 20 elements and a mesh resolution of $h/d = 1$. On the outer wall, a normal traction imposes the wall pressure $P_{\rm wall}$, and the rotational degree of freedom is constrained ($\theta = 0$). On the inner wall, the radial displacement is set to zero ($u_r = 0$), and the rotational degrees of freedom are specified to impose the rotation rate Ω. The vertical degrees of freedom are set to zero for the whole model ($u_z = 0$), and homogeneous Neumann fluidity boundary conditions ($\hat{\zeta} = 0$) are utilized. A mesh size of $h/d = 1/3$ is chosen, and all calculations are run to a total rotation angle of 4° to ensure that steady-state has been attained.

First, we examine the effect of the inner wall rotation rate, $R_{\rm i}\Omega\sqrt{\rho_{\rm s}/P_{\rm wall}}$, fixing the geometry $R_{\rm i}/d = 60$. The tangential velocity fields as a function of r are shown in the main plot of Fig. 3(b) for $R_{\rm i}\Omega\sqrt{\rho_{\rm s}/P_{\rm wall}} = 10^{-4}, 10^{-2}$, and 1. Both the FE and FD solutions are shown, which agree well. As in the case of linear shear with gravity, flow is concentrated in a shear band located at the inner wall with the velocity field decaying as one moves away from the inner wall. The normalized shear

Copyright © 0000 John Wiley & Sons, Ltd.
Prepared using nmeauth.cls

DOI: 10.1002/nme

band width, W/d, as a function of $R_\mathrm{i}\Omega\sqrt{\rho_\mathrm{s}/P_\mathrm{wall}}$ from 10^{-5} to 1 is plotted in the inset of Fig. 3(b). We see a transition from a rate-independent plateau ($R_\mathrm{i}\Omega\sqrt{\rho_\mathrm{s}/P_\mathrm{wall}} \lesssim 10^{-3}$) to a rate-dependent regime ($R_\mathrm{i}\Omega\sqrt{\rho_\mathrm{s}/P_\mathrm{wall}} \gtrsim 10^{-2}$) as the wall velocity is increased. The normalized FE μ-fields are plotted in Fig. 3(c), which compare favorably to the analytical μ-field used in the FD calculations $(92)_3$ and its lack of dependence on the inner wall rotation rate. The wall stress ratio, μ_wall, as a function of $R_\mathrm{i}\Omega\sqrt{\rho_\mathrm{s}/P_\mathrm{wall}}$ from 10^{-5} to 1 is plotted in the inset of Fig. 3(c), showing the transition from a rate-independent plateau of μ_s to a rate-dependent regime as the wall velocity is increased. This transition in both the shear band width W/d and wall stress ratio μ_wall is qualitatively similar to that seen in linear shear with gravity, indicating a transition from rate-independent, nonlocally-dominated flow to rate-dependent flow dominated by the local inertial rheology.

Next, the effect of system size on flow in the rate-independent regime, $R_\mathrm{i}\Omega\sqrt{\rho_\mathrm{s}/P_\mathrm{wall}} = 10^{-3}$, is examined. We consider $R_\mathrm{i}/d = 20, 40, 60, 80$, and 100. The flow fields as a function of r are shown in the main plot of Fig. 3(d) for both FE and FD calculations, verifying the GAX element. The normalized shear band width W/d is plotted in the inset as a function of R_i/d, indicating that the shear band width increases with increasing inner radius. The normalized FE μ-fields are shown in Fig. 3(e), which match well with the corresponding μ-fields used in FD calculations $(92)_3$ for each value of R_i/d. As before, since we are in the rate-independent regime, the wall stress ratio μ_wall remains close to μ_s for all R_i/d. As the inner radius decreases, the gradient in the μ-field increases, and hence flow concentrates into a narrower band. For very large R_i/d, we asymptotically approach a state of simple shear with a constant μ-field, and the shear band would grow to reach the outer wall. However, here we have focused only on situations in which the outer wall has no influence.

Finally, we demonstrate mesh convergence for the GAX element for the case of $R_\mathrm{i}/d = 60$ and $R_\mathrm{i}\Omega\sqrt{\rho_\mathrm{s}/P_\mathrm{wall}} = 10^{-3}$. We utilize an identical approach as in the previous section for assessing convergence. A mesh resolution of $h_\mathrm{exact}/d = 1/90$ is used as the "exact" solution, and mesh resolutions of $h/d = 1/9, 2/9, 1/3, 5/9, 2/3$, and 1 are considered. The L_2-norm of the relative error is calculated as in (91) for the displacement and granular fluidity fields and plotted in Fig. 4(a), demonstrating a faster-than-linear rate of convergence. The wall stress ratio μ_wall determined through nodal reaction forces is plotted as a function of d/h in the inset of Fig. 4(a), showing that the reaction forces converge as well. As we did in the case of linear shear flow with gravity, we also consider the same boundary value problem but with a $g = 0$ boundary condition at the inner wall in order to show that our GAX element continues to be valid when mixed fluidity boundary conditions are employed. Again, a boundary layer at the wall occurs, necessitating the same range of fine mesh resolutions used in the previous section. The results of our convergence test using mixed fluidity boundary conditions is shown in Fig. 4(b), showing that all fields and reaction forces converge as desired. Returning to the homogeneous Neumann fluidity boundary condition case, asymptotically quadratic convergence of the Newton procedure is demonstrated in Fig. 4(c). The normalized L_∞-norms of the displacement and fluidity residuals, $R_u^{(k)}$ and $R_g^{(k)}$, are defined as in the previous section, and plots of $R^{(k+1)}$ versus $R^{(k)}$ for displacement and granular fluidity for ten unique increments (each denoted with a different color) clearly show a quadratic power law, confirming that quadratic convergence is achieved.

6.3. Annular shear flow with gravity

Finally, we consider a more complex flow configuration than in the previous sections – one in which the stress field is not known a priori and hence requires our FE implementation. To this end, we consider annular shear *with* gravity, shown schematically in Fig. 5. The annular cell has rough inner and outer walls of radii R_i and R_o, respectively, and a *smooth* floor, filled to a height H with an open top. Gravity acts in the negative z-direction, and the inner wall is rotated at a rate Ω. Again, we expect flow to be concentrated near the inner wall in a shear band. In this case, the important dimensionless parameters are (i) the dimensionless inner wall radius, R_i/d, and (ii) the dimensionless inner wall velocity, $R_\mathrm{i}\Omega/\sqrt{Gd}$. We take $(R_\mathrm{o} - R_\mathrm{i}) = 20d$, which is large enough so that the flow field is independent of the outer wall radius. Finally, we take $H/d = 15$, although this parameter has no effect on the flow field for the smooth-floor case.

Copyright © 0000 John Wiley & Sons, Ltd.
Prepared using nmeauth.cls

DOI: 10.1002/nme

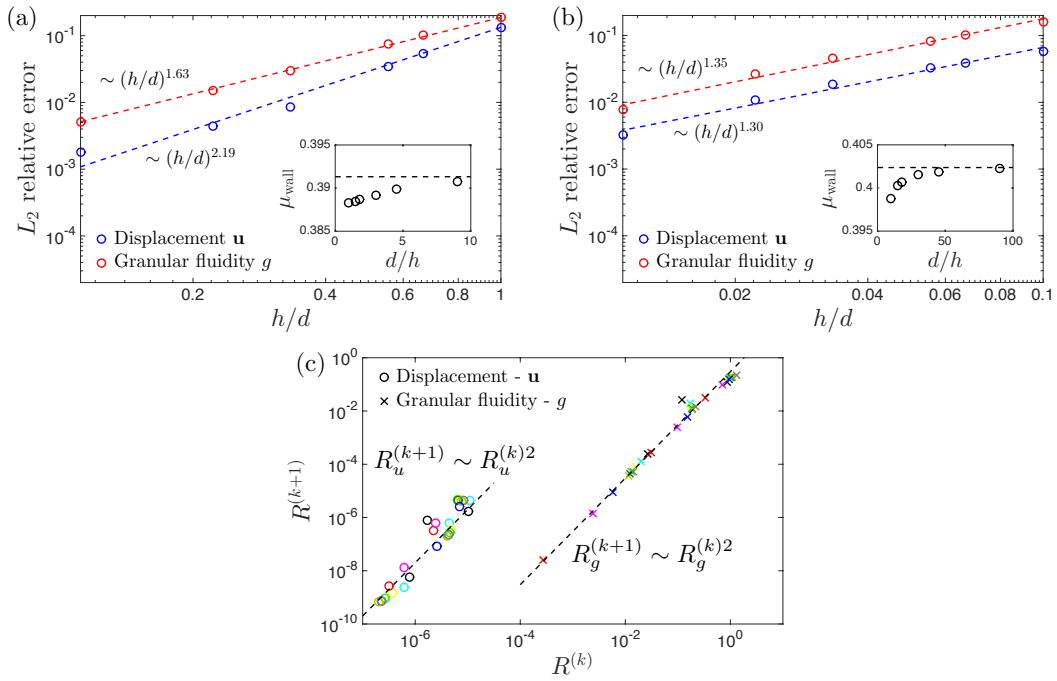

Figure 4. (a) Demonstration of convergence for annular shear flow without gravity for $R_{\rm i}/d = 60$ and $R_{\rm i}\Omega\sqrt{\rho_{\rm s}/P_{\rm wall}} = 10^{-3}$. L_2-norm of the relative error as a function of the normalized mesh resolution h/d for the displacement and granular fluidity fields. Inset: Normalized wall reaction force $\mu_{\rm wall}$ as a function of mesh resolution. The "exact" solution is denoted by the horizontal dashed line. (b) Convergence test repeated for the case of a homogeneous Dirichlet ($g = 0$) wall fluidity boundary condition. (c) Demonstration of asymptotically quadratic convergence of the Newton procedure. The colors of the markers denote unique increments, and the dashed lines denote a quadratic power law.

We consider both GAX and 3D FE meshes and will show that indistinguishable results are obtained for both elements. The GAX mesh is shown in Fig. 5(a) for a 60 by 45 element mesh and a mesh resolution of $h/d = 1/3$. On the outer wall, the radial displacement and rotational degrees of freedom are constrained ($u_r = \theta = 0$). On the inner wall, the radial displacement is set to zero ($u_r = 0$), and the rotational degrees of freedom are specified to impose the rotation rate Ω. For the 3D mesh, a narrow slice of the annulus (total angle $0.1°$) is simulated using periodic boundary conditions on the front and back faces – nodal displacements on the front face are constrained to be identical to those on the back face except rotated appropriately by $0.1°$, and nodal fluidities on the front face are constrained to be identical to those on the back face. The slice is modeled using a slab of elements, which is one element thick in the θ-direction. Regarding side-wall displacement boundary conditions in the 3D mesh, the displacements in the r- and θ-directions are prescribed to match the given wall motion – stationary for the outer wall and rotating at a rate of Ω for the inner wall. For both GAX and 3D meshes, material may slide without resistance up and down the walls, but the vertical degrees of freedom are set to zero ($u_z = 0$) on the floor, while the radial displacement and rotational degrees of freedom are left unconstrained. The top surface is traction-free, and homogeneous Neumann fluidity boundary conditions ($\hat{\zeta} = 0$) are specified on all boundaries in the r-z-plane for both GAX and 3D meshes. For the subsequent results, we use a mesh size of $h/d = 1/3$ and run all calculations to a total rotation angle of $4°$ to ensure that steady-state has been attained.

Again, we begin by examining the effect of inner wall rotation rate, $R_{\rm i}\Omega/\sqrt{Gd}$, at a fixed geometry of $R_{\rm i}/d = 60$. The normalized tangential velocity fields on the top surface ($z = H$) as a function of r/d are shown in the main plot of Fig. 5(b) for $R_{\rm i}\Omega/\sqrt{Gd} = 10^{-4}, 10^{-2}$, and 1.

Copyright © 0000 John Wiley & Sons, Ltd.
Prepared using nmeauth.cls

DOI: 10.1002/nme

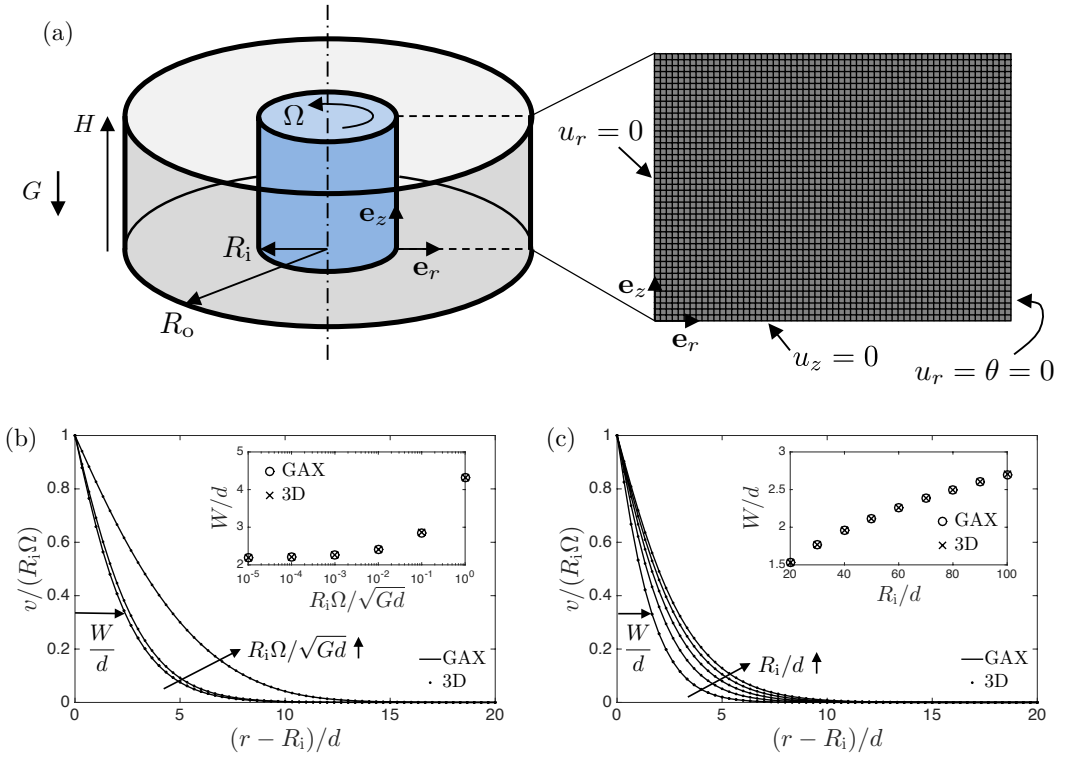

Figure 5. Simulation results for annular shear flow with gravity. (a) Schematic and finite-element mesh for the GAX element. (b) Surface flow fields obtained from GAX and 3D FE calculations for $R_\mathrm{i}/d = 60$ and $R_\mathrm{i}\Omega/\sqrt{Gd} = 10^{-4}, 10^{-2}$, and 1. Inset: Normalized shear band width W/d as a function of $R_\mathrm{i}\Omega/\sqrt{Gd}$. (c) Surface flow fields in the rate-independent regime ($R_\mathrm{i}\Omega/\sqrt{Gd} = 10^{-3}$) for $R_\mathrm{i}/d = 20, 40, 60, 80$, and 100. Inset: Normalized shear band width as a function of R_i/d.

Both GAX and 3D solutions are shown, which are indistinguishable. We see the familiar flow field consisting of a shear band located at the inner wall, decaying into the bulk, with wider shear bands corresponding to faster driving rates. The size of the shear band, characterized by the shear band width, W/d, as a function of $R_\mathrm{i}\Omega/\sqrt{Gd}$ from 10^{-5} to 1 is plotted in the inset of Fig. 5(b), indicating the transition from a rate-independent regime ($R_\mathrm{i}\Omega/\sqrt{Gd} \lesssim 10^{-3}$) to a rate-dependent regime ($R_\mathrm{i}\Omega/\sqrt{Gd} \gtrsim 10^{-2}$) as the wall velocity is increased. To illustrate to full flow fields in each of these regimes, in Fig. 6, we show contour plots of the normalized tangential velocity at steady state, $v/(R_\mathrm{i}\Omega)$, the normalized pressure field, $\bar{p}/(\phi\rho_\mathrm{s}GH)$, and the stress ratio, μ, in the r-z-plane for representative rate-independent ($R_\mathrm{i}\Omega/\sqrt{Gd} = 10^{-3}$) and rate-dependent ($R_\mathrm{i}\Omega/\sqrt{Gd} = 1$) cases. The velocity field in the rate-independent case shows virtually no z-dependence, while the wider shear band in the rate-dependent case only shows a very slight z-dependence. For both cases, the pressure fields are indistinguishable and given by a z-dependent hydrostatic field. The difference between the two cases is much more evident when the μ-fields are examined. In the rate-independent case, the μ-field is nominally independent of z and only just reaches μ_s at the inner wall, indicating that the majority of the domain undergoing flow is *below* its yield condition. As discussed prior, the nonlocal relation, $\nabla^2 g = g/\xi^2$, becomes mathematically rate-independent under these conditions, and hence virtually identical μ-fields are observed for slower driving rates, $R_\mathrm{i}\Omega/\sqrt{Gd} < 10^{-3}$. As the wall speed is increased, the μ-field changes character and shows dependence on both the r and z coordinates. In this regime, much of the domain is above its yield condition, and hence, the local inertial rheology, through the g_loc-term in (23), plays the dominant role. Indeed, similar μ-fields in the rate-dependent regime have been observed in calculations of annular shear flow using the local-only model (see Fig. 5(d) of [4]).

Copyright © 0000 John Wiley & Sons, Ltd.
Prepared using nmeauth.cls

DOI: 10.1002/nme

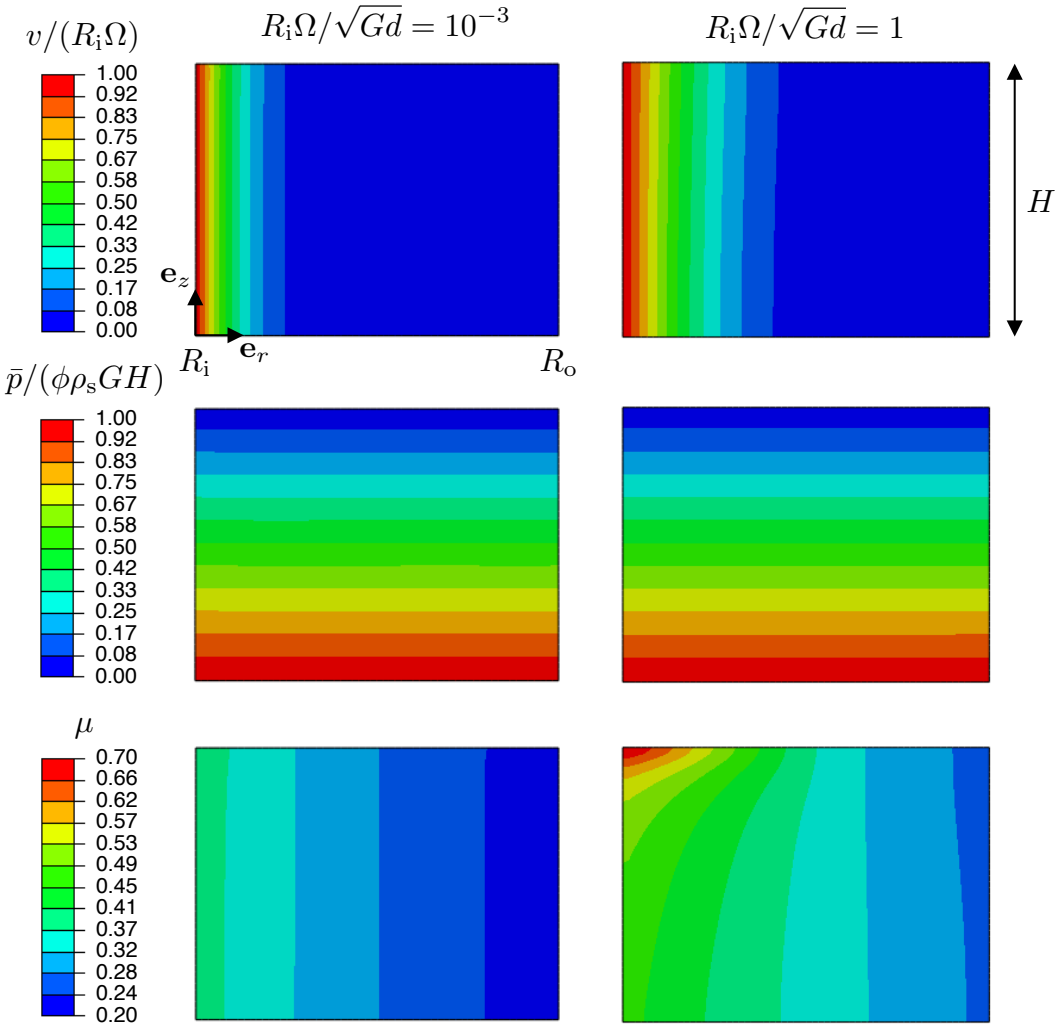

Figure 6. Contour plots of the normalized tangential velocity field, $v/(R_\mathrm{i}\Omega)$, the normalized pressure field, $\bar{p}/(\phi\rho_\mathrm{s}GH)$, and the stress ratio field, μ, in the r-z-plane for representative rate-independent ($R_\mathrm{i}\Omega/\sqrt{Gd} = 10^{-3}$) and rate-dependent ($R_\mathrm{i}\Omega/\sqrt{Gd} = 1$) cases – all at steady-state.

Next, we demonstrate the effect of system size on flow in the rate-independent regime, $R_\mathrm{i}\Omega/\sqrt{Gd} = 10^{-3}$. Flow fields on the top surface as a function of r/d are shown in the main plot of Fig. 5(c) for $R_\mathrm{i}/d = 20, 40, 60, 80$, and 100, for both GAX and 3D meshes, which again yield indistinguishable results. The size of wall-located shear band, characterized by the normalized shear band width, W/d, is plotted in the inset as a function of R_i/d. We see that the shear band width increases with inner wall radius, which may be rationalized in a similar (but not identical) manner as in the previous section. Again, here we have focused on situations in which the outer wall radius has no effect on the flow field. We note that our model has been shown to be quantitatively predictive in this flow configuration for the case of $R_\mathrm{i}/d = 68$ (see Fig. 4(a) of [14] for a comparison to the data of [63]).

Finally, in order to clearly demonstrate the mesh-independence of our solutions, we directly compare calculations obtained using the nonlocal model to calculations under identical conditions but using the local-only model ($g = g_\mathrm{loc}$). First, we fix geometry, $R_\mathrm{i}/d = 60$, and mesh resolution, $h/d = 1/3$, and vary the wall speed for $R_\mathrm{i}\Omega/\sqrt{Gd} = 10^{-4}, 10^{-2}$, and 1. The normalized tangential

Copyright © 0000 John Wiley & Sons, Ltd.
Prepared using nmeauth.cls

DOI: 10.1002/nme

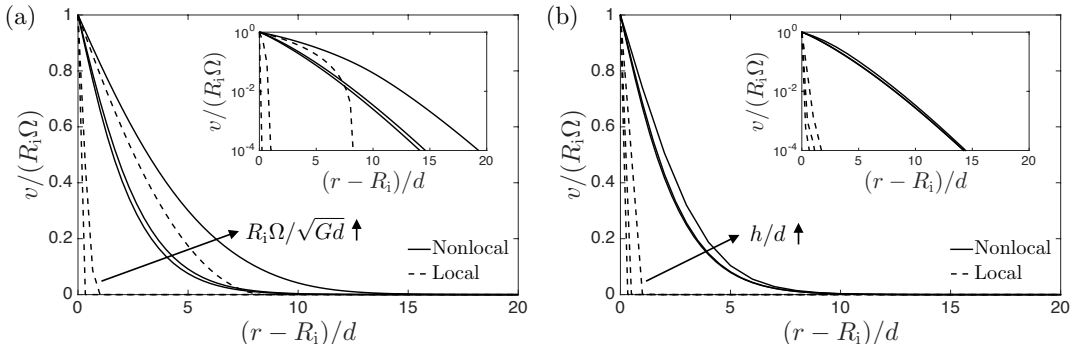

Figure 7. Comparison of nonlocal and local models in annular shear flow with gravity. (a) Surface flow fields for $R_\mathrm{i}/d = 60$, $h/d = 1/3$, and $R_\mathrm{i}\Omega/\sqrt{Gd} = 10^{-4}, 10^{-2}$, and 1. Local model predictions lack a rate-independent plateau. Inset: Replotted in log scale. Local model lacks a exponentially-decaying flow field. (b) Surface flow fields for $R_\mathrm{i}/d = 60$, $R_\mathrm{i}\Omega/\sqrt{Gd} = 10^{-3}$, and $h/d = 1/3, 1/2$, and 1. Nonlocal calculations are mesh-independent, while local calculations are mesh-dependent. Inset: Replotted in log scale.

velocity fields at $z = H$ are shown in Fig. 7(a). The nonlocal results are identical to those in Fig. 5(b); however, the local predictions are markedly different in two important ways:

1. The local model shows no rate-independent plateau regime, with shear band width continuing to decrease as $R_\mathrm{i}\Omega/\sqrt{Gd}$ is decreased. Once the shear band width is comparable to the mesh resolution, the calculation results become mesh-dependent, as is the case for $R_\mathrm{i}\Omega/\sqrt{Gd} = 10^{-4}$ and 10^{-2} cases shown in Fig. 7(a).
2. The local model predicts a strictly elastic, non-flowing response beyond a certain radial position, which is contrary to experimental observation [1, 63, 64], in which an exponential-like decay of the velocity field is seen. This is made clear in the log-scale plot of the velocity fields in the inset of Fig. 7(a), which show predictions of the local model going precisely to zero at some value of r, while the nonlocal predictions exhibit decaying behavior.

Next, we fix geometry, $R_\mathrm{i}/d = 60$, and wall speed in the rate-independent regime, $R_\mathrm{i}\Omega/\sqrt{Gd} = 10^{-3}$, and vary the mesh resolution. Flow fields for mesh resolutions of $h/d = 1/3, 1/2$, and 1 are shown in Fig. 7(b) for both nonlocal and local models. The nonlocal model demonstrates mesh independent solutions, while predicted flow fields using the local model localize to a single element for all resolutions.

7. CONCLUSION

In this paper, we have presented a finite-element-based numerical approach for the nonlocal granular fluidity model. In our approach, the standard nodal degrees of freedom, the displacements, are joined by a new nodal degree of freedom, the granular fluidity, and both the displacement and granular fluidity fields are interpolated using simple, linear C^0-continuous shape functions. The differential relation (3) in addition to the equilibrium equations are then used to define residuals, and we have derived a straightforward implicit time-integration of the model along with algorithmically-consistent tangents. The numerical simulation capability was then been applied to three inhomogeneous flow configurations: (i) linear shear with gravity, (ii) annular shear without gravity, and (iii) annular shear with gravity. Through these simulations, we have verified our implementation, demonstrated convergence, and shown that solutions are mesh-independent, in contrast to a local approach. It bears noting that we have observed no evidence of numerical instabilities or spurious oscillation patterns in our calculations. Since the model has shown promise in predicting granular flows [14, 16], we expect that the ability to robustly solve these equations will be of use to researchers working in the field, and hence, we have made all Abaqus UEL subroutines

Copyright © 0000 John Wiley & Sons, Ltd.

Prepared using nmeauth.cls
DOI: 10.1002/nme

and input files available as supporting information. One possible limitation of the approach is that it does not smoothly transition to the local case. The limit $A \to 0$ is equivalent to dropping the first and last terms from the fluidity residual $(35)_2$, and the resulting numerical system is not robust. Hence, for completeness, we have also included an implementation of the strictly local model, which does not rely on the introduction of the fluidity, in the posted UEL codes.

Looking ahead, this work sets the stage for other implementations involving nonlocal fluidity models:

1. First, it is straightforward to modify the approach for pressure-insensitive materials by removing the dependence on pressure in the definition of the fluidity and in the local flow rule [6]. This case is significantly simpler since the shear and volumetric responses are completely decoupled.
2. Our quasi-static finite-element approach may also be modified to account for dynamic, inertial effects, which can arise in rapid flows, by utilizing the equations of motion instead of the equations of equilibrium (26).
3. Finally, our approach may be modified to use the full dynamical differential relation for the fluidity (21) instead of the system specialized for steady-state (23). A residual based upon (21) takes the form

$$(\mathbf{R}_g)^A = \int_{\mathcal{B}^e} \left[\frac{\partial g}{\partial \mathbf{x}} \cdot \frac{\partial N^A}{\partial \mathbf{x}} + N^A \left(t_0 \dot{g} + (\mu_s - \mu) g + b \sqrt{\frac{\rho_s d^2}{\bar{p}}} \mu g^2 \right) \right] dv - \int_{\mathcal{S}^e_\zeta} \left(N^A \check{\zeta} \right) da. \tag{93}$$

This next step is significant because, while the steady-state form of the nonlocal granular fluidity model used in the present work is capable of predicting the widths of grain-size dependence of flow features and provides mesh-independent solutions, it cannot quantitatively predict the size-dependence of yield seen in granular systems [58, 59, 1]. As we have shown [57], the nonlocal fluidity model based upon (21) is capable of predicting such effects.

Developing numerical simulation capabilities for these extensions will be the focus of future work.

ACKNOWLEDGEMENT

D.L.H. acknowledges funds from the Brown University School of Engineering, and K.K. acknowledges funds from NSF-CBET-1253228 and the MIT Department of Mechanical Engineering.

REFERENCES

1. Midi GDR. On dense granular flows. *Euro. Phys. Journ. E.* 2004; **14**:341–365.
2. da Cruz F, Emam S, Prochnow M, Roux J, Chevoir F. Rheophysics of dense granular materials: Discrete simulation of plane shear flows. *Phys. Rev. E.* 2005; **72**:021 309.
3. Jop P, Forterre Y, Pouliquen O. A constitutive law for dense granular flows. *Nature* 2006; **441**:727.
4. Kamrin K. Nonlinear elasto-plastic model for dense granular flow. *Int. J. Plasticity* 2010; **26**:167–188.
5. Fenistein D, van Hecke M. Wide shear zones in granular bulk flow. *Nature* 2003; **425**:256.
6. Goyon J, Colin A, Ovarlez G, Ajdari A, Bocquet L. Spatial cooperativity in soft glassy flows. *Nature* 2008; **454**(7200):84–87.
7. Koval G, Roux JN, Corfdir A, Chevoir F. Annular shear of cohesionless granular materials: From the inertial to quasistatic regime. *Phys. Rev. E* 2009; **79**:021 306.
8. Picard G, Ajdari A, Lequeux F, Bocquet L. Slow flows of yield stress fluids: Complex spatiotemporal behavior within a simple elastoplastic model. *Phys. Rev. E* 2005; **71**.
9. Bocquet L, Colin A, Ajdari A. Kinetic theory of plastic flow in soft glassy materials. *Phys. Rev. Lett.* 2009; **103**:036 001.
10. Goyon J, Colin A, Bocquet L. How does a soft glassy material flow: finite size effects, non local rheology, and flow cooperativity. *Soft Matter* 2010; **6**:2668–2678.
11. Sollich P, Lequeux F, Hébraud P, Cates M. Rheology of soft glassy materials. *Phys. Rev. Lett.* 1997; **78**:2020–2023.
12. Katgert G, Tighe BP, Möbius ME, van Hecke M. Couette flow of two-dimensional foams. *Europhys. Lett.* 2010; **90**:54 002.
13. Kamrin K, Koval G. Nonlocal constitutive relation for steady granular flow. *Phys. Rev. Lett.* 2012; **108**:178 301.
14. Henann DL, Kamrin K. A predictive, size-dependent continuum model for dense granular flows. *PNAS* 2013; **110**:6730–6735.

Copyright © 0000 John Wiley & Sons, Ltd.
Prepared using nmeauth.cls

DOI: 10.1002/nme

15. Henann DL, Kamrin K. Continuum thermomechanics of the nonlocal granular rheology. *Int. J. Plasticity* 2014; **60**:145–162.
16. Henann DL, Kamrin K. Continuum modeling of secondary rheology in dense granular materials. *Phys. Rev. Lett.* 2014; **113**:178 001.
17. Vardoulakis I, Aifantis EC. A gradient flow theory of plasticity for granular media. *Acta Mechanica* 1991; **87**:197–217.
18. de Borst R, Mühlhaus HB. Gradient-dependent plasticity: Formulation and algorithmic aspects. *Int. J. Numer. Meth. Eng.* 1992; **35**:521–539.
19. Al Hattamleh O, Muhunthan B, Zbib HM. Gradient plasticity modelling of strain localization in granular materials. *Int. J. Numer. Anal. Meth. Geomech.* 2004; **28**:465–481.
20. Gurtin ME, Anand L. A theory of strain-gradient plasticity for isotropic, plastically irrotational materials. part ii: Finite deformations. *J. Mech. Phys. Solids* 2005; **21**:2297–2318.
21. Engelen RAB, Geers MGD, Baaijens FPT. Nonlocal implicit gradient enhanced elasto-plasticity for the modeling of softening behavior. *Int. J. Plasticity* 2003; **19**:403–433.
22. Anand L, Aslan O, Chester SA. A large-deformation gradient theory for elastic-plastic materials: Strain softening and regularization of shear bands. *Int. J. Plasticity* 2012; **30-31**:116–143.
23. Mühlhaus HB, Vardoulakis I. The thickness of shear bands in granular materials. *Géotechnique* 1987; **37**:271–283.
24. de Borst R. Simulation of strain localization: A reappraisal of the cosserat continuum. *Eng. Computation* 1991; **8**:317–332.
25. Mohan LS, Rao KK, Nott PR. A frictional cosserat model for the slow shearing of granular materials. *J. Fluid Mech.* 2002; **457**:377–409.
26. Sun W, Kuhn MR, Rudnicki JW. A multiscale dem-lbm analysis on permeability evolutions inside a dilatant shear band. *Acta Geotech.* 2013; **8**:465–480.
27. Abaqus. Reference manuals. Dassault Systèmes Simulia Corp. 2013.
28. Gurtin ME, Fried E, Anand L. *The Mechanics and Thermodynamics of Continua*. Cambridge, 2010.
29. Kröner E. Allgemeine kontinuumstheorie der versetzungen und eigenspannungen. *Arch. Ration. Mech. Anal.* 1960; **4**:273–334.
30. Lee EH. Elastic plastic deformation at finite strain. *J. Appl. Mech.* 1969; **36**:1–6.
31. Gurtin ME, Anand L. The decomposition $\mathbf{F} = \mathbf{F}^{\mathrm{e}}\mathbf{F}^{\mathrm{p}}$, material symmetry, and plastic irrotationality for solids that are isotropic-viscoplastic or amorphous. *Int. J. Plasticity* 2005; **21**:1686–1719.
32. Aranson IS, Tsimring LS. Continuum theory of partially fluidized granular flows. *Phys. Rev. E* 2002; **65**:061 303.
33. Kamrin K, Bazant MZ. Stochastic flow rule for granular materials. *Phys. Rev. E* 2007; **75**:041 301.
34. Jenkins J, Berzi D. Dense inclined flows of inelastic spheres: tests of an extension of kinetic theory. *Granular Matt.* 2010; **12**:151–158.
35. Schoefield A, Wroth P. *Critical State Soil Mechanics*. McGraw-Hill, 1968.
36. Anand L, Gu C. Granular materials: constitutive equations and strain localization. *J. Mech. Phys. Solids* 2000; **28**:1701.
37. Rudnicki JW, Rice JR. Conditions for the localization of deformation in pressure-sensitive and dilatant materials. *J. Mech. Phys. Solids* 1975; **23**:371.
38. Rycroft CH, Kamrin K, Bazant MZ. Assessing continuum hypotheses in simulation of granular flow. *J. Mech. Phys. Solids* 2009; **57**:828–839.
39. Gurtin ME. Generalized ginzburg-landau and cahn-hilliard equations based on a microforce balance. *Physica D* 1996; **92**:178–192.
40. Lois G, Carlson JM. Force networks and the dynamic approach to jamming in sheared granular media. *Euro. Phys. Lett.* 2007; **80**:58 001.
41. Lemaitre A, Caroli C. Rate-Dependent Avalanche Size in Athermally Sheared Amorphous Solids. *Phys. Rev. Lett.* 2009; **103**(6):065 501.
42. Dahmen KA, Ben-Zion Y, Uhl JT. A simple analytic theory for the statistics of avalanches in shear granular materials. *Nat. Phys.* 2011; **7**:554–557.
43. Kamrin K, Koval G. Effect of particle surface friction on nonlocal constitutive behavior of flowing granular media. *Comput. Part. Mech.* 2014; **1**:169–176.
44. Armero F. Formulation and finite element implementation of a multiplicative model of coupled poro-plasticity at finite strains under fully saturated conditions. *Comput. Method Appl. M.* 1999; **171**:205–241.
45. Andrade JE, Borja RI. Modeling deformation banding in dense and loose fluid-saturated sands. *Finite Elem. Anal. Des.* 2007; **43**:361–383.
46. Chester SA, Di Leo CV, Anand L. A finite element implementation of a coupled diffusion-deformation theory for elastomeric gels. *Int. J. Solids Struct.* 2015; **53**:1–18.
47. Vu DK, Steinmann P, Possart G. Numerical modelling of non-linear electroelasticity. *Int. J. Num. Meth. Eng.* 2007; **70**:685–704.
48. Henann DL, Chester SA, Bertoldi K. Modeling of dielectric elastomers: Design of actuators and energy harvesting devices. *J. Mech. Phys. Solids* 2013; **61**:2047–2066.
49. Miehe C, Welschinger F, Hofacker M. Thermodynamically consistent phase-field models of fracture: Variational principles and multi-field fe implementations. *Int. J. Num. Meth. Eng.* 2010; **83**:1273–1311.
50. Borden MJ, Verhoosel CV, Scott MA, Hughes TJR, Landis CM. A phase-field description of dynamic brittle fracture. *Comput. Method Appl. M.* 2012; **217–220**:77–95.
51. de Souza Neto EA, Perić D, Dutko M, Owen DRJ. Design of simple low order finite elements for large strain analysis of nearly incompressible solids. *Int. J. Solids Struct.* 1996; **33**:3277–3296.
52. de Souza Neto EA, Perić D, Owen DRJ. *Computational Methods for Plasticity: Theory and Applications*. Wiley, 2008.
53. Weber G, Anand L. Finite deformation constitutive equations and a time integration procedure for isotropic, hyperelastic-viscoplastic solids. *Comput. Meth. Appl. Mech. Eng.* 1990; **79**:173–202.

Copyright © 0000 John Wiley & Sons, Ltd.
Prepared using nmeauth.cls

DOI: 10.1002/nme

54. Sun W. A unified method to predict diffuse and localized instabilities in sands. *Geomech. and Geoeng.* 2013; **8**:65–75.
55. Divoux T, Fardin MA, Manneville S, Lerouge S. Shear banding of complex fluids. arXiv:1503.04130 [cond-mat.soft] 2015.
56. Forterre Y, Pouliquen O. Long-surface-wave instability in dense granular flows. *J. Fluid Mech.* 2003; **486**:21–50.
57. Kamrin K, Henann DL. Nonlocal modeling of granular flows down inclines. *Soft Matter* 2015; **11**:179–185.
58. Pouliquen O. Scaling laws in granular flows down rough inclined planes. *Phys. Fluids* 1999; **11**:542.
59. Silbert LE, Landry JW, Grest GS. Granular flow down a rough inclined plane: transition between thin and thick piles. *Phys. Fluids* 2003; **15**:1.
60. Mansard V, Bocquet L, Colin A. Boundary conditions for soft glassy flows: slippage and surface fluidization. *Soft Matter* 2014; **10**:6984–6989.
61. Artoni R, Richard P. Effective wall friction in wall-bounded 3d dense granular flows. *Phys. Rev. Lett.* 2015; **115**:158 001.
62. Siavoshi S, Orpe AV, Kudrolli A. Friction of a slider on a granular layer: nonmonotonic thickness dependence and effect of boundary conditions. *Phys. Rev. E* 2006; **73**:010 301(R).
63. Losert W, Bocquet L, Lubensky TC, Gollub JP. Particle dynamics in sheared granular matter. *Phys. Rev. Lett.* 2000; **85**:1428–1431.
64. Mueth DE, Debregeas GF, Karczmar GS, Eng PJ, Nagel SR, Jaeger HM. Signatures of granular microstructure in dense shear flows. *Nature* 2000; **406**:385–388.

Copyright © 0000 John Wiley & Sons, Ltd.
Prepared using nmeauth.cls

DOI: 10.1002/nme